Vaz-Romero, A.; Rotbaumb, Y.; Rodríguez-Martínez, J.A.; Rittel, D. (2016). Necking evolution in dynamically stretched bars: New experimental and computational insights. *Journal of the Mechanics and Physics of Solids*, vol. 91, June 2016, pp. 216-239.

DOI: https://doi.org/10.1016/j.jmps.2016.02.024

Necking evolution in dynamically stretched bars: New experimental and computational insights

A. Vaz-Romero[a], Y. Rotbaum[b], J. A. Rodríguez-Martínez[a,*], D. Rittel[b]

[a] *Department of Continuum Mechanics and Structural Analysis. University Carlos III of Madrid. Avda. de la Universidad, 30. 28911 Leganés, Madrid, Spain*
[b] *Technion Faculty of Mechanical Engineering, Technion, Haifa, 32000, Israel*

Abstract

This paper presents new results on dynamic neck evolution in steel bars of varying diameters. Dynamic tensile tests were carried out in a Kolsky apparatus using cylindrical steel specimens with various cross-section diameters ranging from 1.5 mm to 4 mm. A high speed digital camera was used to record the deformation of the specimen during the loading process. Video recording of the tests enabled accurate experimental measurements of the necking evolution, specifically its growth rate as a function of the diameter. The experiments show that increasing the specimen cross-section slows down the neck development. This behaviour has been further investigated using two different kinds of numerical calculations: (1) axisymmetric finite element simulations and (2) one-dimensional finite difference computations. While the finite difference model only considers the normal stress along the longitudinal direction of the bar, the finite element model does not entail any simplification on the stress state of the specimen during the loading process. In agreement with the experiments, the finite element calculations show a decrease of the necking growth rate with the increase in the cross-section of the sample. On the contrary, the damping effect of the specimen cross-section on the necking evolution is not captured by the finite difference computations. We postulate that this result comes from the one-dimensional nature of the finite difference model. This work uncovers, by means of combined experiments and modelling, the key role played by stress multiaxiality in the growth rate of dynamic necks.

Keywords:

Dynamic necking, Necking growth rate, Dynamic tensile experiments, Numerical calculations, Stress multiaxiality

*Corresponding author. Tel. +34 916248460; Fax: +34 916249430. E-mail address: jarmarti@ing.uc3m.es

1. Introduction

The investigation of necking in ductile rods started with the work of Considère (1885) who proposed the well-known load maximum criterion: necking begins when the increment of strain hardening becomes equal to the geometric softening in a simple tension test. The postulate of Considère predicts the onset of the instability, but says nothing about the evolution of the neck. On the other hand, despite the enormous popularity that this criterion has achieved, it is only applicable to strain rate and temperature insensitive materials tested under quasi-static loading conditions. For several decades, the latter constraint hampered the study of necking in all of kinds applications where the role of inertial forces is not negligible.

For instance, in the 30's and 40's, a series of experimental papers published by Mann (1936, 1937) and Clark and co-workers (Clark and Datwyler, 1938; Clark, 1942; Duwez and Clark, 1947; Clark and Duwez, 1948) showed that the concepts of ductile failure under static loading no longer apply in the dynamic regime. The experiments revealed that the necking inception in a metallic rod subjected to impact loading is controlled, to a large extent, by the intervention of strain propagation phenomena within the specimen. These authors concluded that, for most metallic materials, the ultimate strength and ductility under dynamic loading are different from those observed under quasi-static conditions.

Nevertheless, it took a long time to build a theoretical framework to describe necking inception under dynamic loading. In the 80's, Fressengeas and Molinari (1985, 1994), based on previous works of Hill and Hutchinson (1975) and Hutchinson et al. (1978), developed a linear stability analysis which uncovered the critical mechanisms controlling the necking inception at high strain rates. These authors showed that inertia and stress multiaxiality effects stabilize the material behaviour and delay the onset of necking. The later works of Shenoy and Freund (1999), Mercier and Molinari (2003, 2004) and Zhou et al. (2006) confirmed the findings of Fressengeas and Molinari (1985, 1994). It is apparent that the analytical solutions obtained from the linear stability analyses provide important information on the localization behaviour of uniformly strained solids. However, they fall short of describing the onset of instability in specimens subjected to wave propagation phenomena. In this case, due to the strongly non-linear nature of the problem, a full numerical solution of the field equations is required.

The numerical studies on the dynamic necking problem started in the late 80's and early 90's

with the pioneering works of Regazzoni et al. (1986), Needleman and co-workers (Tvergaard and Needleman, 1990; Needleman, 1991; Knoche and Needleman, 1993) and Nemes and Eftis (1993). One advantage of the numerical calculations is that, unlike the linear stability analyses, they allow to investigate the spatio-temporal development of the instability. For two decades the numerical methods have been the most common tool to analyze dynamic problems which involve localization of plastic deformations. For instance, the papers of Noor et al. (1998), Sørensen and Freund (1998), Guduru and Freund (2002), Xue et al. (2008), Mirone (2013) and Rotbaum et al. (2015) studied the evolution of the field variables in necked regions of viscoplastic bars subjected to dynamic tension. These works suggested that the multidimensional character of the stress, strain and strain rate fields which develop inside a neck control, to a large extent, the post-uniform behaviour of the specimen. The numerical calculations indicated that material inertia introduces a length scale so that the specimen ductility is a function of the specimen size. It was shown that the inception and evolution of dynamic necks depend on structural aspects such as load and boundary conditions as much as on the properties of the material.

However, only the latest developments in high-speed image recording enabled the experimental verification of these numerical findings. In the recent works of Tarigopula et al. (2008), Gilat et al. (2009), Besnard et al. (2012) and Sato et al. (2015), the digital image correlation technique was used to extract the strain fields during the post-uniform elongation of dynamic tensile specimens. The stress-strain relation and the strain rate history in the necking region were determined in order to obtain dynamic material characteristics at large strains. These papers reported the first experimental evidences of the high levels (and large gradients) of strain and strain rate that develop inside dynamic necks.

In the present paper we also perform high-speed image recording of dynamic tensile tests, however, our purpose is different. We aim at measuring, for the first time in the literature, the growth rate of dynamic necking instabilities. For that task, we conducted dynamic tension experiments in a Kolsky apparatus using cylindrical steel specimens with various cross-section diameters ranging from 1.5 mm to 4 mm. We monitored the central cross-section of the necked region and obtained, as a function of the specimen diameter, the speed at which the necking develops. These experiments revealed a significant reduction of the necking growth rate with the increase of the sample cross-section. This behaviour has been further investigated using two different kinds of numerical

calculations: (1) axisymmetric finite element simulations and (2) one-dimensional finite difference computations. While the finite element model does not entail any simplification on the stress state in the specimen during the loading process, the finite difference model only considers the normal stress along the longitudinal direction of the bar. As opposed to the experiments and the finite element calculations, the necking growth rate predicted by the finite difference model is insensitive to the sample diameter. This key outcome demonstrates the critical role played by the stress multiaxiality in the evolution of a dynamic neck. While such a result was devised in several of the above-mentioned theoretical works, our combined experimental-numerical results are the first, to the authors' knowledge, to confirm earlier predictions.

2. Material and mechanical characterization

2.1. Material

The material of this study is AISI 304L (cold drawn) austenitic stainless steel. This grade is one of the most versatile and widely used stainless steels. Type 304L is an extra low-carbon variation of AISI 304. 304L steel serves in a wide range of applications (including the transportation sector and the petrochemical and nuclear industries) because of its strength, work hardening, excellent formability and large ductility. The latter is an essential feature for our investigation, and the main reason for selecting this material: large ductility implies well developed necks prior to fracture.

The chemical composition of the AISI 304L is given in Table 1.

Fe	**C**	**Mn**	**P**	**S**	**Si**	**Cr**	**Ni**	**N**
Balance	0.03 max.	2.00 max.	0.045 max.	0.03 max.	0.75 max.	18.00 - 20.00	8.00 - 12.00	0.1

Table 1: *Chemical composition of the AISI 304L stainless steel (wt %), as taken from AK steel corporation (2007).*

The material was supplied as a 12.7 mm bar from which the specimens (compression and tension, see sections 2.2 and 4.1) were machined.

2.2. Mechanical characterization

We conducted quasi-static (at various temperatures) and dynamic compression tests to characterize the strain, strain rate and temperature dependences of the material flow stress. The cylindrical specimens were machined with diameter 6 mm and length 6 mm. In accordance with

Davies and Hunter (1963) and Malinowski and Klepaczko (1986), a length-to-diameter ratio of 1 was chosen to minimize spurious friction and inertia effects. In addition, the contact interfaces of the samples were lubricated using molybdenum disulfide grease.

2.2.1. Quasi-static tests

The quasi-static experiments were conducted using a screw-driven machine (Instron 4483) under displacement control. A laser optical extensometer ($LE-05$, EIR) was used for axial strain measurements.

The quasi-static experiments at room temperature were conducted at three nominal (initial) strain rates: $\dot{\varepsilon}_0 = 10^{-3}\ s^{-1}$, $\dot{\varepsilon}_0 = 10^{-2}\ s^{-1}$ and $\dot{\varepsilon}_0 = 10^{-1}\ s^{-1}$. Fig. 1 shows a room temperature characteristic for $10^{-2}\ s^{-1}$ which reveals the high initial yield stress $\approx 700\ MPa$ and work hardening of the material. Note that, at room temperature, the stress-strain characteristic is convex up to $\varepsilon \approx 0.1$, beyond which it turns (slightly) concave. The slight concavity is maintained until $\varepsilon \approx 0.2$, when it becomes convex again. Such a specific strain hardening is caused by the martensitic transformation which is characteristic of this steel at low strain rates and room temperature. A detailed analysis on the kinetics and thermodynamics of the martensitic transformation in 304 steel can be found in previous works of the authors (Rodríguez-Martínez et al., 2011; Zaera et al., 2012, 2013). Nevertheless, in this paper our interest is limited to the macroscopic response of the material while setting aside any discussion about the underlying microstructural mechanisms.

The quasi-static tests at elevated temperatures were carried out at $\dot{\varepsilon}_0 = 10^{-2}\ s^{-1}$. Fig. 1 shows that the stress-strain characteristic is slightly shifted downwards as the testing temperature increases, revealing the temperature sensitivity of the material within the investigated range of test temperatures.

2.2.2. Dynamic tests

The dynamic compression experiments were performed using a conventional 19.7 mm diameter Kolsky apparatus made of C300 hardened Maraging steel bars. The experiments were conducted within the range of strain rates $2400\ s^{-1} \lesssim \dot{\varepsilon}_0 \lesssim 4300\ s^{-1}$. The stress, strain and strain rate in the specimen were calculated from the recorded time-dependent strains of the bars following the conventional procedure (Kolsky, 1949). Equilibrium was checked for each sample, and corrections for wave dispersion were applied using a home-made program according to the procedure described

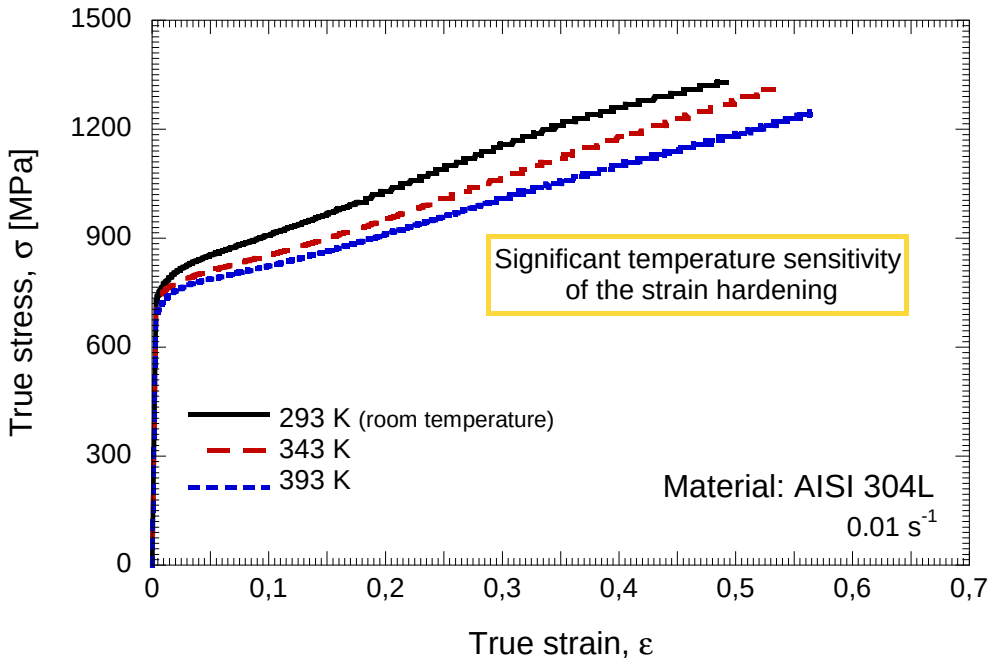

Figure 1: Experimental stress-strain curves for AISI 304L at $\dot{\varepsilon}_0 = 0.01\ s^{-1}$. Three different initial temperatures are investigated: $T = 293\ K$, $T = 343\ K$ and $T = 393\ K$.

by Lifshitz and Leber (1994).

Fig. 2 shows typical stress-strain curves obtained at different loading rates. Dynamic experimental curves for $\dot{\varepsilon}_0 = 3750\ s^{-1}$ and $\dot{\varepsilon}_0 = 4050\ s^{-1}$ are compared with a stress-strain characteristic obtained for $\dot{\varepsilon}_0 = 0.01\ s^{-1}$. While the flow stress increases only moderately with the strain rate, the dynamic strain hardening shows a significant reduction when $\varepsilon \geq 0.4$. The stress-strain characteristics under dynamic loading are no longer convex/concave/convex as in the static case, but they are *simply* convex. We argue that adiabatic heating at high strain rates and large strains reduces the amount of austenite transformed into martensite during the course of plastic deformation (Zaera et al., 2013), which lowers the strain hardening of the material.

3. Constitutive modelling

The material behaviour is described by a hypoelastic-plastic constitutive model which follows the standard principles of Huber-Mises plasticity: additive decomposition of the rate of deformation tensor, isotropic hardening, associated flow rule and plastic power equivalence.

The evolution equation for the Kirchhoff stress $\boldsymbol{\tau}$ is:

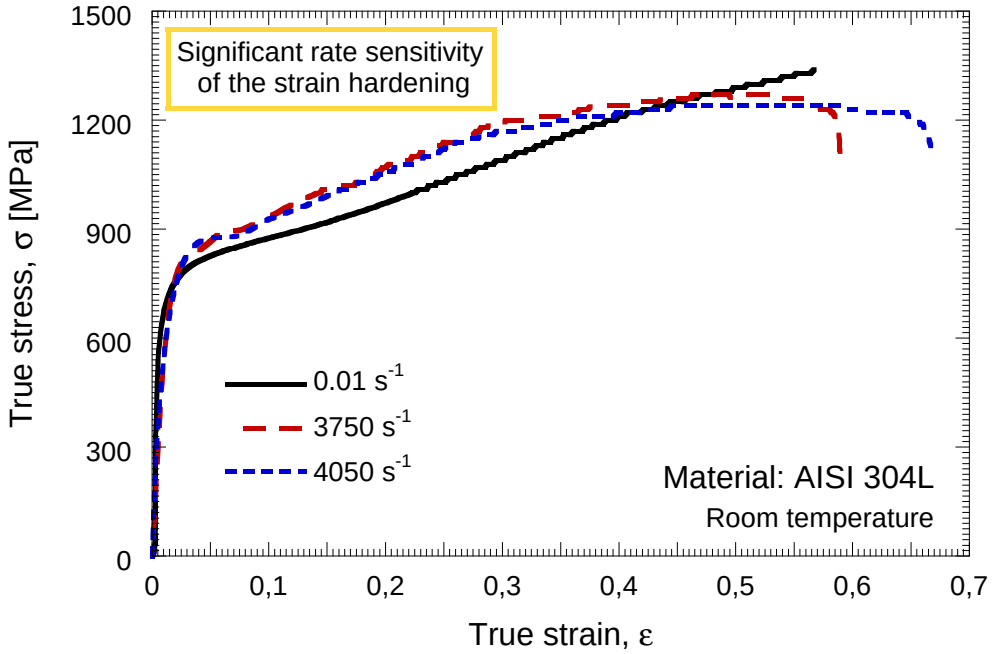

Figure 2: Experimental stress-strain curves for AISI 304L at room temperature. Three different initial strain rates are investigated: $\dot{\varepsilon}_0 = 0.01\ s^{-1}$, $\dot{\varepsilon}_0 = 3750\ s^{-1}$ and $\dot{\varepsilon}_0 = 4050\ s^{-1}$.

$$\boldsymbol{\tau}^{\nabla} = \mathcal{L} : \mathbf{d}^{\mathrm{e}} \tag{1}$$

where $\boldsymbol{\tau}^{\nabla}$ is an objective derivative of the Kirchhoff stress tensor. The fourth order isotropic elasticity tensor $\mathcal{L}$ and the elastic rate of deformation tensor $\mathbf{d}^{\mathrm{e}}$ are defined as follows:

$$\mathcal{L} = 2G\mathcal{I} + \eta \mathbf{I} \otimes \mathbf{I} \tag{2}$$

$$\mathbf{d}^{e} = \mathbf{d} - \mathbf{d}^{p} \tag{3}$$

where G and η are the Lamé's constants, $\mathcal{I}$ is the fourth order identity tensor and $\mathbf{I}$ is the second order identity tensor. $\mathbf{d}$ and $\mathbf{d}^{\mathrm{p}}$ are the total and plastic rate of deformation tensors, respectively.

The yield function Ψ is written as:

$$\Psi = \bar{\tau} - \sigma_Y = 0 \tag{4}$$

where the Huber-Mises equivalent stress $\bar{\tau}$ and the yield stress σ_Y are defined as follows:

$$\bar{\tau} = \sqrt{\frac{3}{2}\left(\mathbf{s} : \mathbf{s}\right)} \tag{5}$$

$$\sigma_Y = A + B\left(\bar{\varepsilon}^p\right)^h \left(\frac{\dot{\bar{\varepsilon}}^p}{\dot{\bar{\varepsilon}}_{ref}}\right)^m \left(\frac{T}{T_{ref}}\right)^{-\mu} \tag{6}$$

where $\mathbf{s} = \boldsymbol{\tau} - \frac{1}{3}\left(\boldsymbol{\tau} : \mathbf{I}\right)\mathbf{I}$ is the deviatoric part of the Kirchhoff stress, $\dot{\bar{\varepsilon}}^p = \sqrt{\frac{2}{3}\left(\mathbf{d}^{\mathrm{p}} : \mathbf{d}^{\mathrm{p}}\right)}$ is the equivalent plastic strain rate, $\bar{\varepsilon}^p = \int_0^t \dot{\bar{\varepsilon}}^p\left(\xi\right)\mathrm{d}\xi$ is the equivalent plastic strain and T is the temperature. A, B, h, m and μ are material parameters while $\dot{\bar{\varepsilon}}_{ref}$ and T_{ref} are the reference strain rate and temperature, respectively. The identification of the yield stress parameters is conducted by a numerical regression procedure based on the compression experiments performed at different strain rates and temperatures.

The flow rule is given by:

$$\mathbf{d}^{\mathrm{p}} = \frac{\partial \Psi}{\partial \boldsymbol{\tau}} \dot{\bar{\varepsilon}}^p = \frac{3}{2}\frac{\mathbf{s}}{\bar{\tau}} \dot{\bar{\varepsilon}}^p \tag{7}$$

The formulation of the model is completed by introducing the Kuhn–Tucker loading/unloading complementary conditions:

$$\dot{\bar{\varepsilon}}^p \geq 0, \quad \Psi \leq 0, \quad \dot{\bar{\varepsilon}}^p \Psi = 0 \tag{8}$$

and the consistency condition during plastic loading:

$$\dot{\Psi} = 0 \tag{9}$$

Physical constants, elastic parameters and parameters related to the yield stress for AISI 304L steel are given in Table 2.

Symbol	**Property and units**	**Value**
ρ_o	Initial density (kg/m^3)	8030
C_p	Specific heat (J/kgK), Eqs. (12) and (29)	500
k	Thermal conductivity (W/mK), Eqs. (12) and (29)	16.2
G	Lamé's constant (GPa), Eqs. (2), (15), (17) and (18)	75.2
η	Lamé's constant (GPa), Eq. (2)	146
A	Initial yield stress (MPa), Eq. (6)	820.58
B	Work hardening modulus (MPa), Eq. (6)	1356.73
h	Work hardening exponent, Eq. (6)	0.871
$\dot{\bar{\varepsilon}}_{ref}$	Reference strain rate (s^{-1}), Eq. (6)	0.001
m	Strain rate sensitivity exponent, Eq. (6)	0.0105
T_{ref}	Reference temperature (K), Eq. (6)	293
μ	Temperature sensitivity exponent, Eq. (6)	2.093
β	Taylor-Quinney coefficient, Eqs. (12) and (29)	0.9

Table 2: *Elastic parameters and parameters related to the yield stress for AISI 304L steel. The physical constants are taken from AK steel corporation (2007).*

The authors are aware that this simple constitutive model does not consider some specific features of the mechanical response of the AISI 304L. For instance, as mentioned in section 2.2.1, we do not account explicitly for the martensitic transformation. Thus, the model does not capture the concave part of the static stress-strain characteristics and neglects the slight mechanical anisotropy induced by the strain-induced phase transformation (Zaera et al., 2012). Nevertheless, we claim that the simple modelling presented here is sufficient to develop reliable numerical computations to uncover the critical factors which control the necking growth rate in the dynamic tensile test (see sections 5.2 and 6.3). For a more sophisticated constitutive modelling of the steel 304 the reader is referred to previous papers of the authors (Zaera et al., 2012, 2013) in which the strain induced martensitic transformation is (explicitly) accounted for.

4. Analysis and results: Experiments

4.1. Experimental setup

The dynamic tensile experiments were performed using a standard 12.7 mm diameter Kolsky tensile apparatus (Kolsky, 1949; Harding et al., 1960) made of C300 hardened Maraging steel bars. The apparatus was loaded using a 400 mm long tubular projectile, launched toward a flange located at the end of the incident bar. In order to prevent from specimen reloading, a momentum trap was brought initially in contact with the loaded flange of the incident bar, whose length was identical to that of the projectile bar. Further details of the experimental arrangement can be found in Rittel et al. (2014) and Rotbaum and Rittel (2014). Moreover, a Kirana high speed digital camera was synchronized with the incident bar signals to record the deformation of the specimen during the loading process. As further discussed in section 4.2, the image recording of the tests enables accurate experimental measurements of the necking growth rate, as a basis for comparison with numerical modelling.

The geometry, dimensions and mechanical boundary conditions of the cylindrical samples (round cross-section) used in the dynamic tensile experiments are given in Fig. 3. While the gauge length was kept constant for all the samples, $L = 8\ mm$, specimens with 4 different cross-section areas were tested: type 1 with cross-section diameter $\Phi = 1.5\ mm$, type 2 with $\Phi = 2\ mm$, type 3 with $\Phi = 3\ mm$ and type 4 with $\Phi = 4\ mm$. One should note the experimental restrictions on the choice of specimen diameters. As the diameter gets reduced, the signal transmitted through the specimen diminishes to an extent that, for diameters below 1.5 mm, the signal to noise ratio is too low to obtain a reliable measured signal. On the other hand, when the diameter exceeds 4 mm, the amount of strain imparted to the specimen diminishes so that one could only observe the onset of necking, with limited growth. Note that, for all the samples tested, the ratio L/Φ is greater than unity which, according to Matic et al. (1988), allows to fully developed necking. The input and output applied velocities (mechanical boundary conditions v^{inp} and v^{out}) were determined from the measured incident, reflected and transmitted pulses, as for any other standard test with the Split Hopkinson Tensile Bar. Note that Osovski et al. (2013) showed that this apparatus leads to applied velocities at both ends of the sample. For all the experiments performed the nominal strain rate is largely similar, lying within the range $1800\ s^{-1} \leq \dot{\varepsilon}_0 \leq 2200\ s^{-1}$.

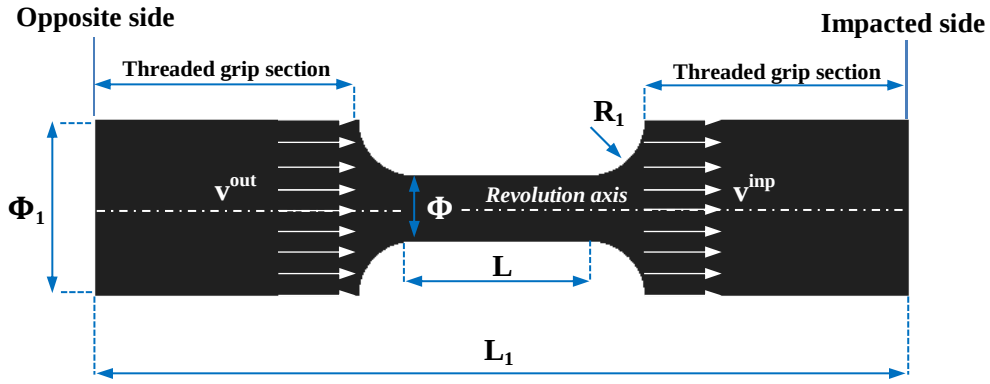

Type 1				
L_1	L	Φ_1	Φ	R_1
36	8	8	1.5	3.25

Type 2				
L_1	L	Φ_1	Φ	R_1
36	8	8	2	3

Type 3				
L_1	L	Φ_1	Φ	R_1
36	8	8	3	2.5

Type 4				
L_1	L	Φ_1	Φ	R_1
36	8	8	4	2

Figure 3: Geometry, dimensions and mechanical boundary conditions of the specimens used in the dynamic tensile experiments. All dimensions are given in mm.

4.2. Experimental results

Figs. 4 and 5 show the normalized axial force $\bar{F} = \frac{F}{\Lambda_0}$ as a function of the loading time t for various experiments. Note that F is the raw force measured in the test and $\Lambda_0 = \frac{\pi\Phi^2}{4}$ is the initial cross-section area of the sample. On the one hand Figs. 4(a) and 4(b) present the results obtained for specimens with cross-section diameters $\Phi = 1.5\ mm$ and $\Phi = 2\ mm$. On the other hand Figs. 5(a) and 5(b) present the results obtained for specimens with $\Phi = 3\ mm$ and $\Phi = 4\ mm$, respectively.

Three distinct tests are shown in each graph to illustrate the repeatability of the experimental measurements. At the first stages of the loading process, an inertial peak appears, followed by some fluctuations in the signal which are mostly caused by the nature of the test in which severe accelerations are applied to the specimen. The inertial peak and the force fluctuations are damped with increased specimen cross-section. In addition, the recorded signal stabilizes earlier as Φ increases. One can attribute this behaviour to the increase of inertial effects with the cross-section diameter. Moreover, we observe that the (stable) normalized force level during the homogeneous deformation of the specimens is largely constant with a value of $\approx 1000\ N/mm^2$. At a later stage of the loading process, the force decays due to the necking inception. In this regard, one must highlight two key issues:

1. Irrespective of the cross-section diameter, the onset of necking occurs within the range $80\ \mu s \lesssim t \lesssim 90\ \mu s$. The increase of Φ causes only a slight delay in the drop of the force. One can surmise that this *delay* is caused by the increase of the inertia effects with the specimen cross-section.
2. The rate of decay of the force depends very strongly on the specimen diameter. The increase of Φ slows down the growth rate of the neck, and (consequently) damps the load drop. The final fracture of the sample, corresponding to $\bar{F} = 0$, occurs at $t \approx 100\ \mu s$ for $\Phi = 1.5\ mm$ and at $t \approx 150\ \mu s$ for $\Phi = 4\ mm$. The time from necking inception to final fracture increases, drastically, with the cross-section diameter.

Fig. 6 shows excerpts of video sequences of the necking and failure processes for two different experimental tests. We selected sample 2 ($\Phi = 1.5\ mm$) and sample 7 ($\Phi = 3\ mm$) since, as shown in Figs. 4 and 5, these two experiments showed very different necking growth rates. In the video sequences, one clearly observes the progressive reduction of the specimen cross-section

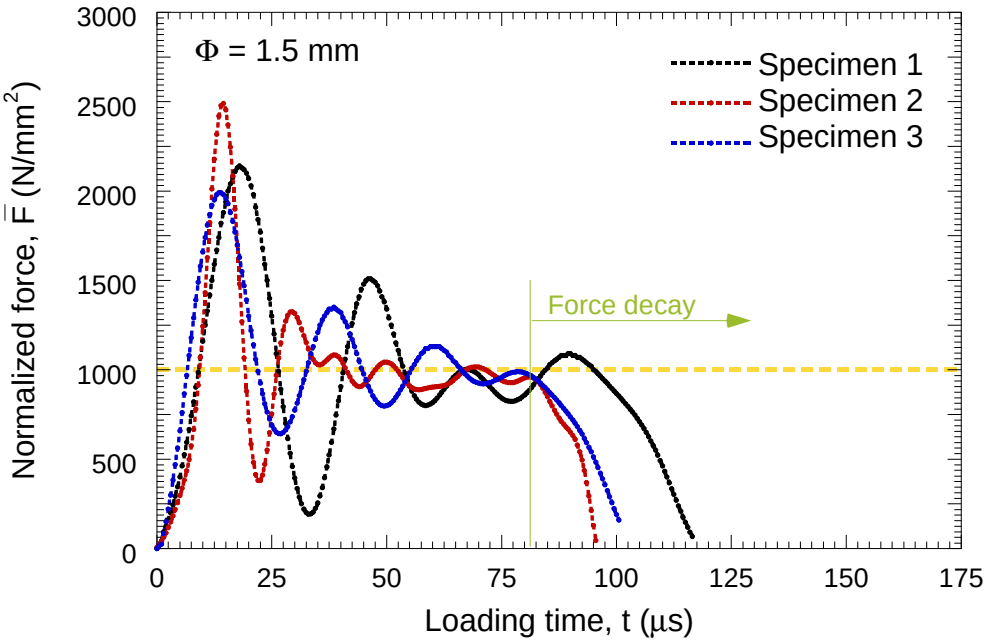

(a)

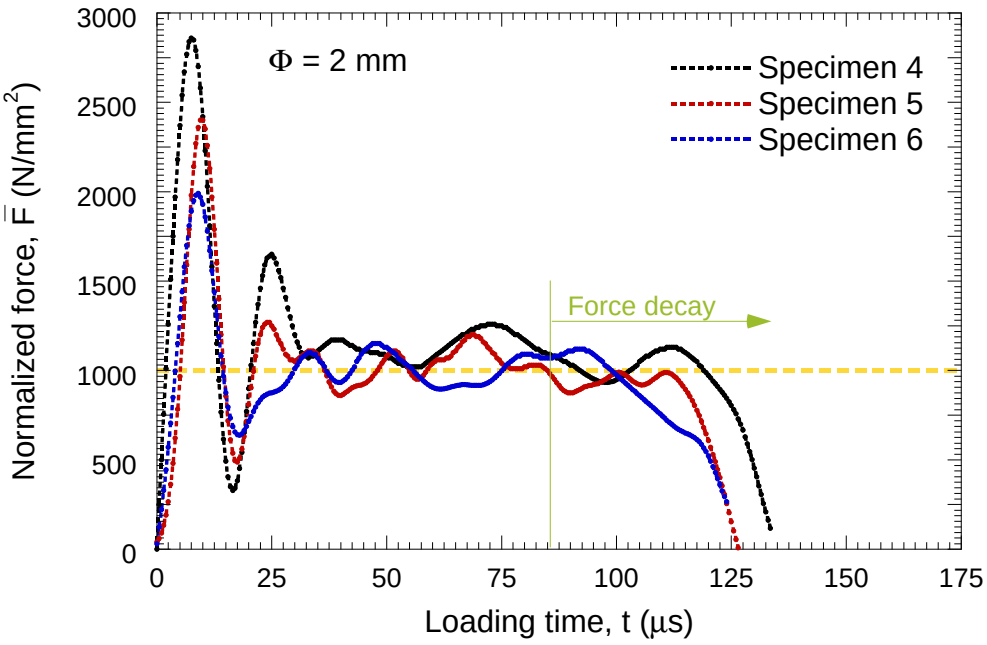

(b)

Figure 4: Experiments. Normalized axial force $\bar{F} = \frac{F}{\Lambda_0}$ as a function of the loading time t for various tests. (a) Three experiments (samples 1, 2 and 3) with cross-section diameter $\Phi = 1.5\ mm$. (b) Three experiments (samples 4, 5 and 6) with cross-section diameter $\Phi = 2\ mm$. The nominal strain rate is similar for all the experiments and lies within the range $1800\ s^{-1} \leq \dot{\varepsilon}_0 \leq 2200\ s^{-1}$.

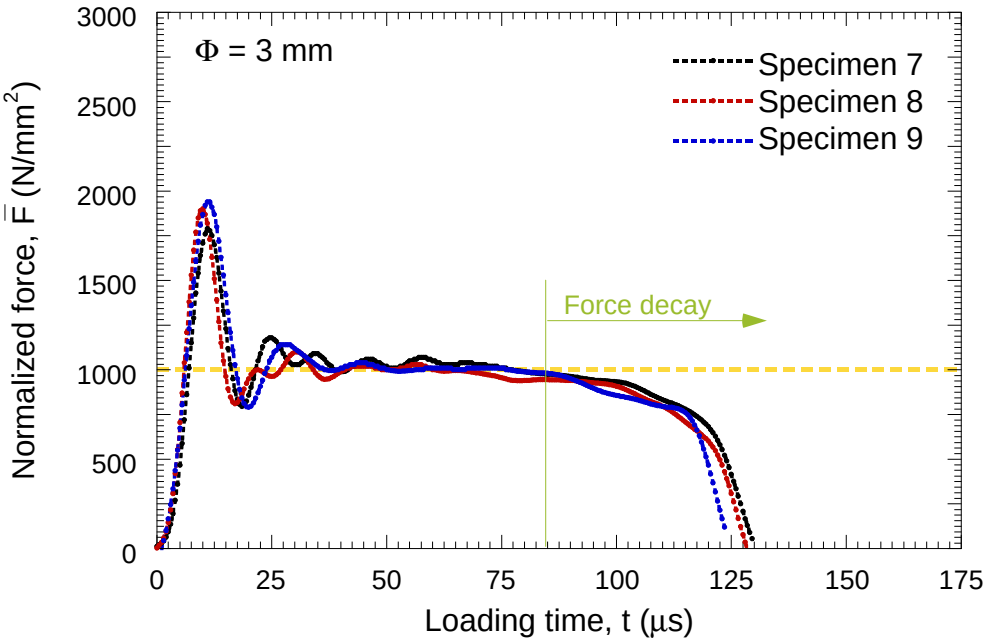

(a)

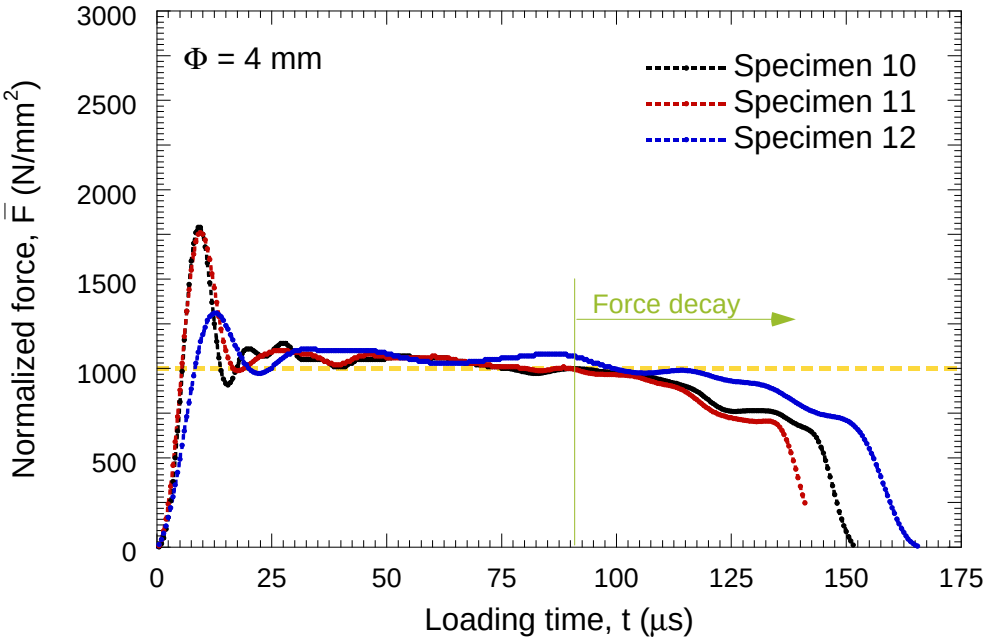

(b)

Figure 5: Experiments. Normalized axial force $\bar{F} = \frac{F}{\Lambda_0}$ as a function of the loading time t for various tests. (a) Three experiments (samples 7, 8 and 9) with cross-section diameter $\Phi = 3\ mm$. (b) Three experiments (samples 10, 11 and 12) with cross-section diameter $\Phi = 4\ mm$. The nominal strain rate is similar for all the experiments and lies within the range $1800\ s^{-1} \leq \dot{\varepsilon}_0 \leq 2200\ s^{-1}$.

which characterizes necking instability. Taking advantage of the elevated acquisition frequency of the video recording (1000000 fps) and the high resolution of the pictures (924 × 768 pixels), we could monitor the current diameter of the specimens during the tests. Specifically, we have focused on the diameter of the central cross-section of the neck in order to evaluate the growth rate of the instability. Details of the procedure are given in Appendix A.

Fig. 7 shows the normalized radial displacement of the central cross-section of the neck $\bar{u}_a = \frac{2u_a}{\Phi - 2u_a}$ versus the loading time t. This dimensionless measure of the radial displacement is especially suited to show the sensitivity of the necking growth rate to the specimen diameter. In Appendix B we demonstrate using Bridgman's analysis (Bridgman, 1944, 1952) that the parameter $\bar{u}_a$ defines the multiaxial stress state in the central cross-section of the neck. Thus, for all purposes, Fig. 7 represents the temporal evolution of the stress state in the necked section. Results are shown for specimens 2 and 7. These are the samples shown in the video sequences of Fig. 6. Note that the displacement u_a is measured at the free surface of the specimens cross-section (see Fig. 6). Two critical observations come out from Fig. 7:

1. Time interval $t \lesssim 80\ \mu s$: We observe a smooth increase of the normalized radial displacement with the loading time. The values of $\bar{u}_a$ are very similar for the two specimens. This time interval corresponds to the homogeneous deformation process. The specimens are subjected to uniaxial tension.
2. Time interval $t \gtrsim 80\ \mu s$: We observe a steep increase of the normalized radial displacement with the loading time. The increase is significantly sharper in the case of specimen 2, which has smaller cross-section diameter. This time interval corresponds to the process of necking growth. The stress state in the necked region is multiaxial, see Appendix B.

A linear approximation can be used to quantify the rate of increase of the radial displacement during the process of necking evolution (the slopes indicated in Fig. 7). Following this procedure, we obtained experimental data of the normalized growth rate of the neck $\frac{d\bar{u}_a}{dt} = \dot{\bar{u}}_a$ as a function of the sample diameter. This is a critical outcome of this paper that, to the authors' knowledge, has not been previously reported in the literature. Fig. 8 shows that $\dot{\bar{u}}_a$ decreases significantly (non-linearly) with the increase of Φ. The multiaxial stress state in the necked region, characterized by the parameter $\bar{u}_a$ as shown in Appendix B, evolves differently depending on the sample diameter. The repeatability in the experimental measurement has to be emphasized.

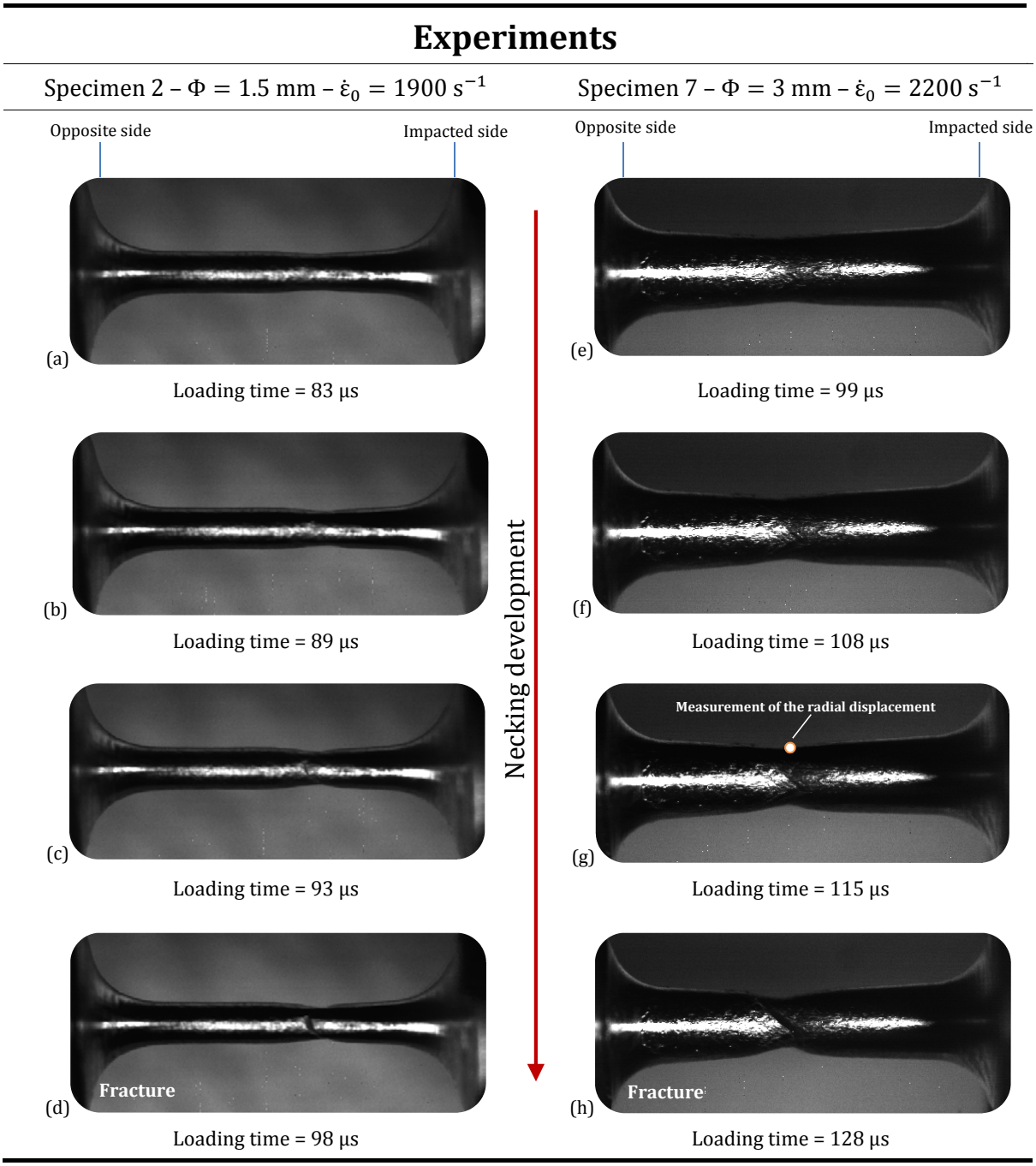

Figure 6: Experiments. Video sequence for two different experimental tests. Specimen 2: $\Phi = 1.5\ mm$ and $\dot{\varepsilon}_0 = 1900\ s^{-1}$. Specimen 7: $\Phi = 3\ mm$ and $\dot{\varepsilon}_0 = 2200\ s^{-1}$. Acquisition frequency: 1000000 frames per second. Image resolution: 924×768 pixels.

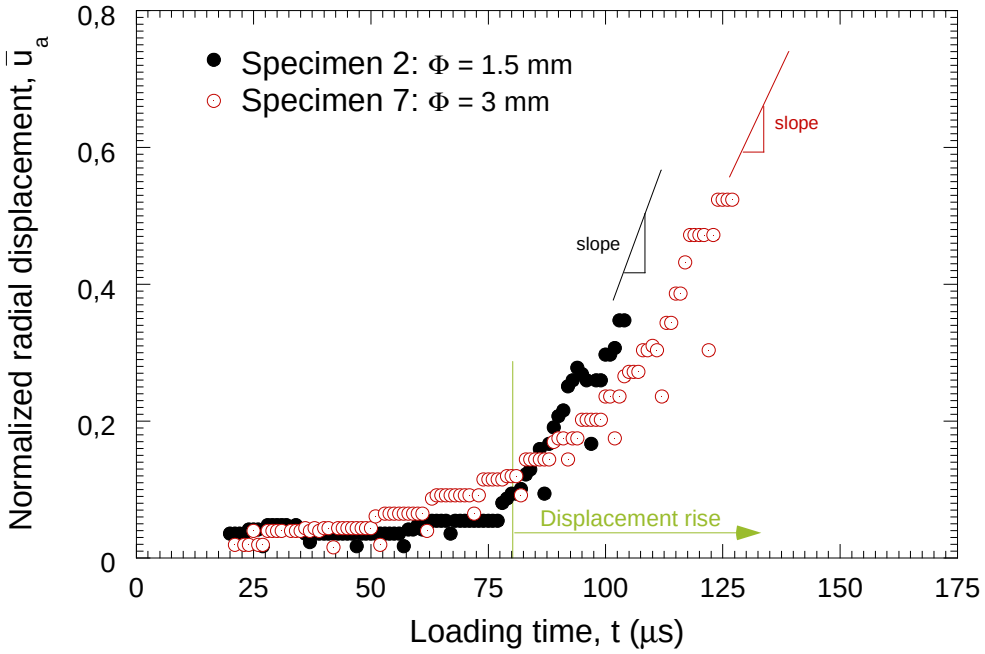

Figure 7: Experiments. Normalized radial displacement of the central cross-section of the neck $\bar{u}_a = \frac{2u_a}{\Phi - 2u_a}$ versus loading time t for two different experimental tests. Specimen 2: $\Phi = 1.5\ mm$ and $\dot{\varepsilon}_0 = 1900\ s^{-1}$. Specimen 7: $\Phi = 3\ mm$ and $\dot{\varepsilon}_0 = 2200\ s^{-1}$.

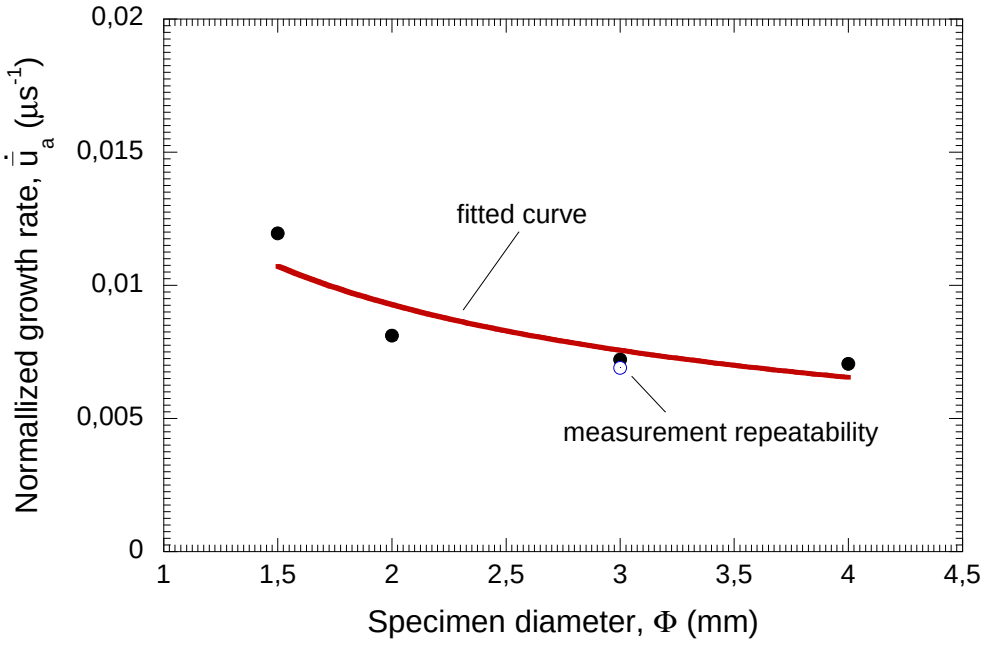

Figure 8: Experiments. Normalized growth rate of the neck $\dot{\bar{u}}_a$ versus diameter of the specimen cross-section Φ. The repeatability in the measurements is highlighted.

The salient feature of the experiments, rather unique within the literature devoted to dynamic tensile necking, is that they provide *quantitative* evidence of the stabilizing role played by the specimen cross-section. Furthermore, we showed that the elongation to failure strongly depends on the sample diameter. These findings are further investigated numerically in the following sections of this paper.

5. Analysis and results: axisymmetric finite element model

Finite element calculations were performed using the code ABAQUS/Explicit (Simulia, 2010) in order to obtain further insights about the experimental outcomes presented above.

5.1. Finite element model

This section describes the features of the axisymmetric finite element model developed to simulate necking in AISI 304L steel bars subjected to dynamic tension. It must be noted that the goal of the numerical calculations is not to mimic the experimental tests but to shed light into the mechanisms which slow down the necking growth rate as the sample diameter increases. For that purpose, simple geometrical models which solely consider the gauge of the sample are sufficient, as further demonstrated in section 5.2. This greatly simplifies the interpretation of the finite element results and reduces the computational cost. Fig. 9 shows the numerical model of a cylindrical bar with initial length $L = 8\ mm$ (the notation is consistent with Fig. 3) subjected to dynamic stretching. We investigate the same cross-section diameters used in the experiments (see Fig. 3).

Note that (R, Z) denotes the Lagrangian coordinate system while (r, z) refers to the Eulerian. The mechanical initial and boundary conditions are:

$$\bar{\tau}(R, Z, 0) = 0; \qquad \bar{\varepsilon}(R, Z, 0) = 0 \tag{10}$$

$$w\,(R, 0, t) = 0\ ; \qquad \dot{w}\,(R, L, t) = v^{inp} = \dot{\varepsilon}_0 L \tag{11}$$

where w is the axial displacement and the superposed dot denotes differentiation with respect to time. Note that, in order to facilitate the interpretation of the finite element results, we have simplified the mechanical boundary conditions (in comparison with the experimental ones shown in Fig. 3) such that $v^{out} = 0$ (i.e. $w\left(R, 0, t\right) = 0$ as stated above).

Moreover, we consider a *fully coupled* thermo-mechanical framework in which the relationship between the spatio-temporal variation of the temperature T and the dissipative heat generation rate is given by:

$$\rho C_p \dot{T} = k\nabla^2 T + \beta \boldsymbol{\tau} : \mathbf{d}^{\mathrm{p}} \tag{12}$$

where ρ is the current material density, C_p is the specific heat, k is the thermal conductivity and β is the Taylor-Quinney coefficient (see Table 2). Note that thermoelastic effects are neglected. Assuming no heat flow at the workpiece boundaries, the thermal initial and boundary conditions are:

$$T\left(R, Z, 0\right) = T_0 \tag{13}$$

$$\frac{\partial T\left(R, 0, t\right)}{\partial Z} = \frac{\partial T\left(R, L, t\right)}{\partial Z} = 0 \; ; \qquad \frac{\partial T\left(0, Z, t\right)}{\partial R} = \frac{\partial T\left(\frac{\Phi}{2}, Z, t\right)}{\partial R} = 0 \tag{14}$$

The finite element models are meshed using four node coupled displacement-temperature axisymmetric elements, with reduced integration and hourglass control ($CAX4RT$). The elements have an initial aspect ratio $1:1$ with dimensions $25 \times 25\ \mu m^2$ for all the models that we have built. According to Zukas and Scheffer (2000), such an element shape is optimal for describing dynamic events like high rate flow localization. A mesh convergence study was performed, in which the time evolution of different critical output variables, namely stress, strain and necking inception, were compared against a measure of mesh density until the results converged satisfactorily. Note that viscosity, inertia and thermal conductivity all act as regularization factors that contribute to the well-possessedness of the problem at hand (Needleman, 1988; Molinari, 1997). We assume that this

minimizes the spurious influence of the mesh in the solution of the boundary value problem.

Note that the use of an axisymmetric finite element model does not entail any simplification on the stress state in the bar during necking. Regarding the stress state in the solid, the finite element computations are fully 3D. This *(obvious)* statement will be critical to understand the comparisons reported in section 6.3 between the axisymmetric finite element computations and one-dimensional calculations carried out using a finite differences scheme.

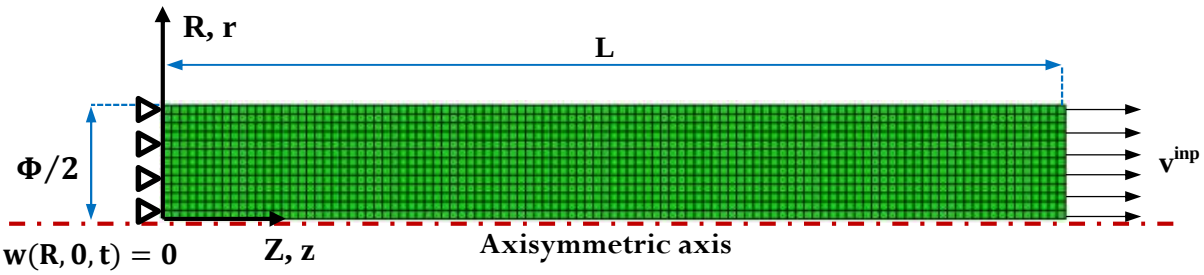

Figure 9: Finite element mesh and mechanical boundary conditions of the cylindrical bar, modelled as an axially symmetric specimen.

The set of constitutive equations given in section 3 are implemented in the finite element code through a user subroutine VUMAT. For its integration in a finite deformation framework, incremental objectivity is achieved by rewriting them in a corotational configuration (Simó and Hughes, 1998; Doghri, 2000), defined in ABAQUS/Explicit by the polar rotation tensor. The stress is updated with the radial return algorithm such that:

$$\boldsymbol{\tau}^{n+1} = \boldsymbol{\tau}^{n+1}_{\text{trial}} - 3G\Delta\bar{\varepsilon}^{p}\frac{\mathbf{s}^{n+1}}{\bar{\tau}^{n+1}} \tag{15}$$

The trial stress is defined as:

$$\boldsymbol{\tau}^{n+1}_{\text{trial}} = \boldsymbol{\tau}^{n} + \mathcal{L} : \Delta\boldsymbol{\varepsilon} \tag{16}$$

where $\Delta\boldsymbol{\varepsilon}$ is the strain increment.

The deviatoric stress is given by:

$$\boldsymbol{s}^{n+1} = \mathcal{I}_{dev}\boldsymbol{\tau}^{n+1} = \boldsymbol{s}_{trial}^{n+1} - 3G\Delta\bar{\varepsilon}^{p}\frac{\boldsymbol{s}^{n+1}}{\bar{\tau}^{n+1}} \tag{17}$$

where $\mathcal{I}_{dev}$ is the deviatoric projector and $\boldsymbol{s}_{trial}^{n+1}$ is the deviatoric part of the trial stress.

The equivalent stress is given by the following expression:

$$\bar{\tau}^{n+1} = \bar{\tau}_{\text{trial}}^{n+1} - 3G\Delta\bar{\varepsilon}^{p} \tag{18}$$

where the relation $\frac{\boldsymbol{s}^{n+1}}{\bar{\tau}^{n+1}} = \frac{\boldsymbol{s}_{trial}^{n+1}}{\bar{\tau}_{trial}^{n+1}}$ has been used.

Therefore, the terms in Eq. (15) are known once the plastic strain increment $\Delta\bar{\varepsilon}^{p}$ is obtained by imposing the consistency condition. For that task, according to Zaera and Fernández-Sáez (2006), we rewrite the consistency condition as follows:

$$\Psi^{n+1} = \Psi\left(\bar{\tau}^{n+1}, (\bar{\varepsilon}^{p})^{n+1}, (\dot{\bar{\varepsilon}}^{p})^{n+1}, T^{n+1}\right) = 0 \tag{19}$$

where the plastic strain rate is approximated as $\dot{\bar{\varepsilon}}^{p} = \frac{\Delta\bar{\varepsilon}^{p}}{\Delta t}$. It has to be noted that, since we use the coupled displacement-temperature approach, the temperature update T^{n+1} is not calculated in the user subroutine but it is given by the finite element code.

Then, we rewrite Eq. (19) as a function of the equivalent plastic strain which leads to a non-linear algebraic equation in $\Delta\bar{\varepsilon}^{p}$:

$$\Psi\left(\bar{\tau}_{\text{trial}}^{n+1} - 3G\Delta\bar{\varepsilon}^{p}, (\bar{\varepsilon}^{p})^{n} + \Delta\bar{\varepsilon}^{p}, \frac{\Delta\bar{\varepsilon}^{p}}{\Delta t}, T^{n} + \Delta T\left(\Delta\bar{\varepsilon}^{p}\right)\right) = 0 \tag{20}$$

In order to implement an iterative Newton-Raphson procedure to find the value of the plastic strain increment, the previous expression is linearised as follows:

$$\Psi^{(f+1)} \approx \Psi^{(f)} - 3G\delta\bar{\varepsilon}^{p(f)} - H^{(f)}\delta\bar{\varepsilon}^{p(f)} - M^{(f)}\frac{\delta\bar{\varepsilon}^{p(f)}}{\Delta t} - P^{(f)}\frac{\beta}{\rho C_p}\left(\bar{\tau}^{n+1}_{\text{trial}}\delta\bar{\varepsilon}^{p(f)} - 6G\Delta\bar{\varepsilon}^{p(f)}\delta\bar{\varepsilon}^{p(f)}\right) = 0 \quad (21)$$

where f is the iteration index, $H = -\frac{\partial\Psi}{\partial\bar{\varepsilon}^p}$ is the plastic modulus, $M = -\frac{\partial\Psi}{\partial\dot{\bar{\varepsilon}}^p}$ is the viscoplastic modulus and $P = -\frac{\partial\Psi}{\partial T}$ is the temperature sensitivity. Note that the linearised term arising from $\Delta T\,(\Delta\bar{\varepsilon}^p)$ (last term in previous equation) can be calculated because it entirely comes from the heat generated due to plastic deformation (see Eq. (12)).

From previous expression we can obtain $\delta\bar{\varepsilon}^{p(f)}$ as:

$$\delta\bar{\varepsilon}^{p(f)} = \frac{\Psi^{(f)}}{3G + H^{(f)} + \frac{M^{(f)}}{\Delta t} + P^{(f)}\frac{\beta}{\rho_0 C_p}\left(\bar{\tau}^{n+1}_{\text{trial}} - 6G\Delta\bar{\varepsilon}^{p(f)}\right)} \quad (22)$$

and $\Delta\bar{\varepsilon}^p$ is updated at the end of the iteration such that:

$$\Delta\bar{\varepsilon}^{p(f+1)} = \Delta\bar{\varepsilon}^{p(f)} + \delta\bar{\varepsilon}^{p(f)} \quad (23)$$

The plastic strain increment $\Delta\bar{\varepsilon}^p$ is obtained after fulfilling the tolerance requirements imposed to the Newton-Raphson procedure. Then, the stress is updated.

In the following section we show the results obtained from the finite element computations. Qualitative comparisons are carried out with the experimental outcomes reported in section 4.2.

5.2. Finite element results

Fig. 10 shows the normalized axial force $\bar{F} = \frac{F}{\Lambda_0}$ as a function of the loading time t for computations with different cross-section diameters $\Phi = 1.5\ mm$, $\Phi = 2\ mm$, $\Phi = 3\ mm$ and $\Phi = 4\ mm$. The impact velocity is $v^{inp} = 16\ m/s$ which corresponds to a nominal strain rate $\dot{\varepsilon}_0 = 2000\ s^{-1}$. This graph is the numerical counterpart of the experimental Figs. 4 and 5. The following key points are noticeable:

1. Time interval $t \lesssim 80\ \mu s$: Corresponds to the homogeneous deformation process. According to our experimental observations, the normalized axial force $\bar{F}$ is largely constant and

barely depends on the value of Φ considered. Note that the value of the (constant) force $\approx$ 920 N/mm^2, is quite similar to the experimentally recorded. The difference, 1000 vs. 920 N/mm^2, is attributed to the simple constitutive model used to describe the mechanical response of the material.

2. Time interval $t \gtrsim 80$ μs: Corresponds to the necking development. According to the experimental observations, the loading time for which the force starts to decay is largely independent of the specimen cross-section. Note that the value $t = 80$ μs is in excellent agreement with the experimental measurements (see Figs. 4 and 5). Furthermore, the drop of the force is significantly slowed down as Φ increases. Note the vast differences in the rate of force decay between $\Phi = 1.5$ mm and $\Phi = 4$ mm.
3. In agreement with the experimental evidences, the elongation to failure is found to be highly dependent on the sample-size. The structural ductility strongly depends on the dimensions of the specimen.

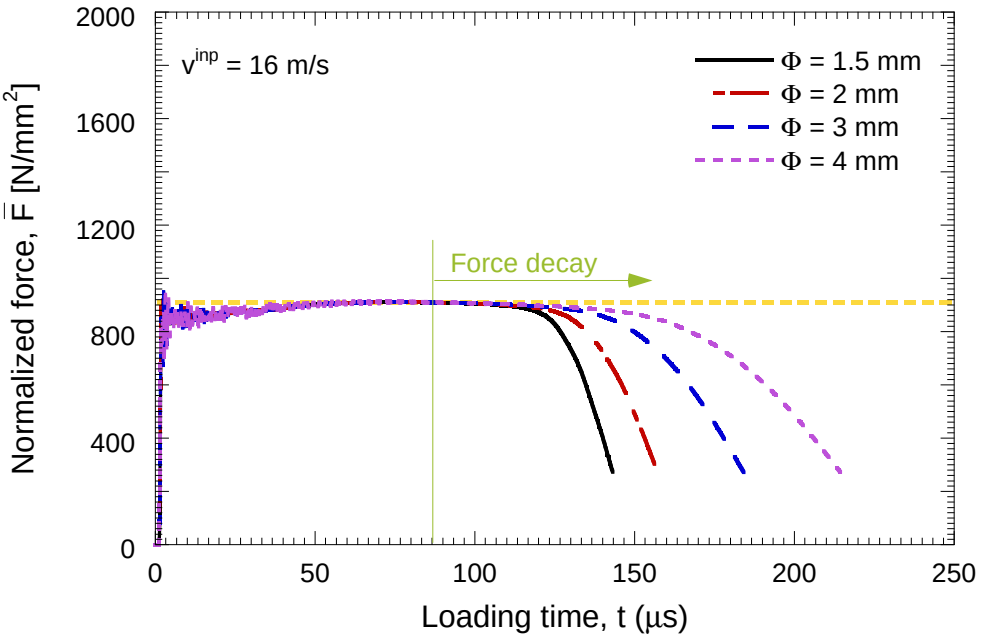

Figure 10: Finite element results. Normalized axial force $\bar{F} = \frac{F}{\Lambda_0}$ upon the loading time t for computations with different cross-section diameters: $\Phi = 1.5$ mm, $\Phi = 2$ mm, $\Phi = 3$ mm and $\Phi = 4$ mm. The impact velocity is $v^{inp} = 16$ m/s which corresponds to a nominal strain rate $\dot{\varepsilon}_0 = 2000$ s^{-1}.

Fig. 11 shows, for the same calculations reported in Fig. 10, the normalized radial displacement $\bar{u}_a$ as a function of the loading time t. The key outcomes are:

1. Time interval $t \lesssim 80$ μs: There is a moderate (and largely constant) increase of the radial

displacement with the loading time. In agreement with the experimental observations, the results are barely dependent on the cross-section diameter. The specimens are subjected to unixial stress state.

2. Time interval $t \gtrsim 80\ \mu s$: There is a significant increase of the radial displacement with the loading time. A multiaxial stress state develops in the necked region. In agreement with the experiments, this increase is substantially sharper as the cross-section diameter decreases. We have used a linear approximation (slopes illustrated in Fig. 11) to obtain a numerical estimation of the necking growth rate.

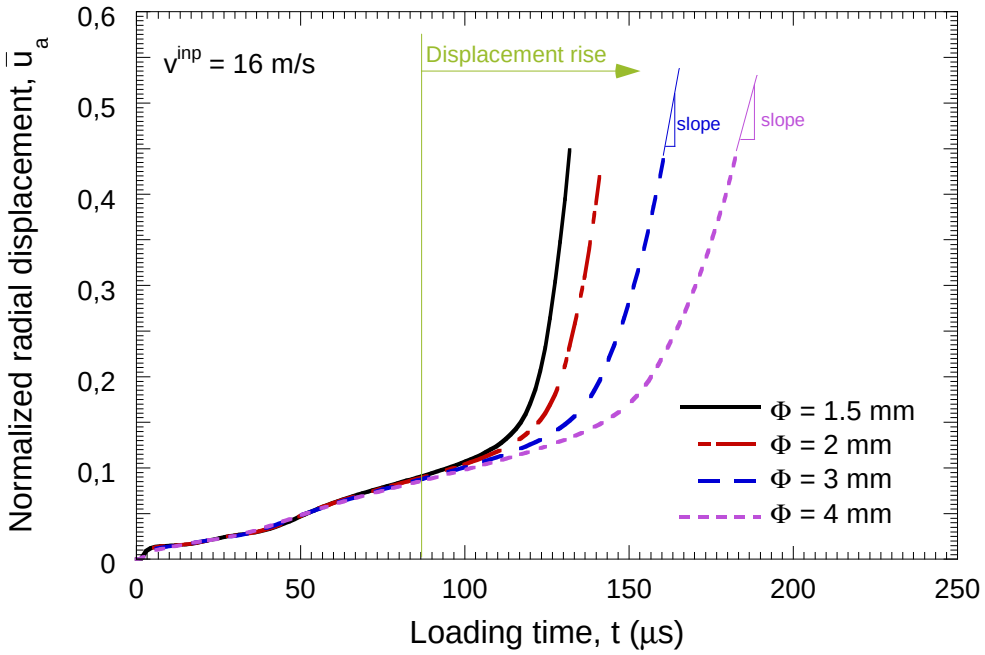

Figure 11: Finite element results. Normalized radial displacement at the necking location $\bar{u}_a = \frac{2u_a}{\Phi - 2u_a}$ upon the loading time t for computations with different cross-section diameters: $\Phi = 1.5\ mm$, $\Phi = 2\ mm$, $\Phi = 3\ mm$ and $\Phi = 4\ mm$. The impact velocity is $v^{inp} = 16\ m/s$ which corresponds to a nominal strain rate $\dot{\varepsilon}_0 = 2000\ s^{-1}$.

The normalized necking growth rates obtained from the finite element computations are shown in Fig. 12. In agreement with the experimental observations (see Fig. 8), the curve $\dot{\bar{u}}_a - \Phi$ shows a decreasing power-type concave up shape. The evolution of the stress state in the necked section depends on the specimen diameter. The influence of the cross-section diameter on the necking grow rate decreases gradually with the increase of Φ. Note that $\dot{\bar{u}}_a$ is three times greater for $\Phi = 1.5\ mm$ than for $\Phi = 4\ mm$.

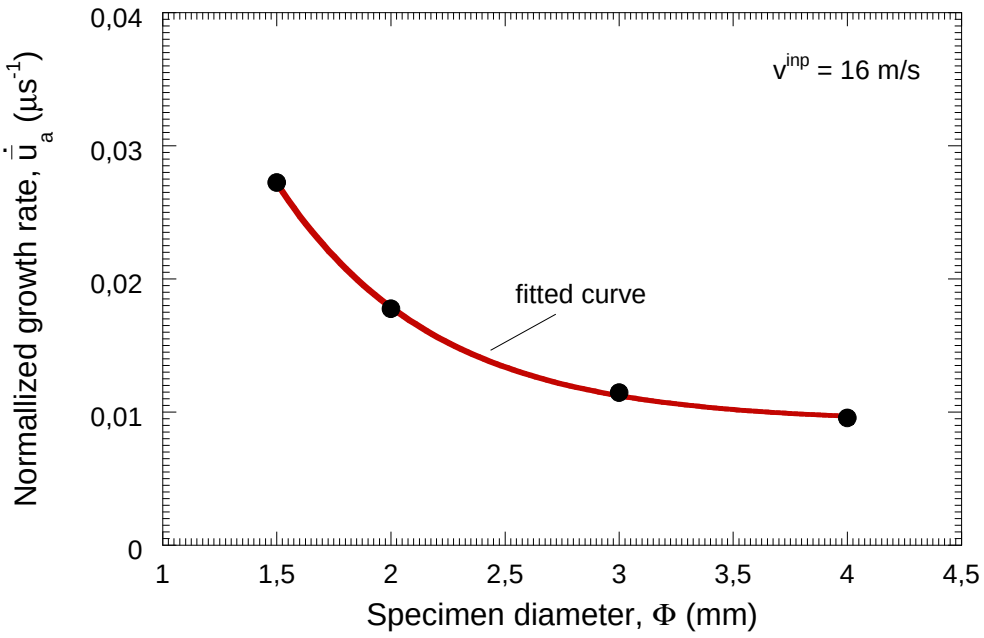

Figure 12: Finite element results. Normalized growth rate of the neck $\dot{\bar{u}}_a$ versus diameter of the specimen cross-section Φ.

The salient feature of the finite element calculations is that they capture the slowdown of the necking growth rate caused by the increase of the specimen cross-section. Further insights into the precise mechanisms that are responsible for the stabilizing role of the diameter of the sample are given in section 6.3.

6. Analysis and results: finite difference model

In this section we develop a simple 1D finite difference model in order to complement the axisymmetric finite element calculations. Note that the 1D model is such because it only considers the normal stress along the longitudinal direction of the bar. The comparison of the results of the axisymmetric and 1D analyses will provide additional information on the stabilizing role played by the sample cross-section in the necking growth rate.

6.1. Governing equations

Similarly to the finite element model presented in section 5.1, we consider a cylindrical bar of initial length $L = 8\ mm$ subjected to dynamic stretching. The relation between the Eulerian z and the Lagrangian coordinate Z $(0 \leq Z \leq L)$ is given by:

$$z = Z + w \tag{24}$$

The logarithmic strain and strain rate along the axial direction are given by:

$$\varepsilon_{zz} = ln\left(\lambda_{zz}\right) = ln\left(1 + \partial w/\partial Z\right) \tag{25}$$

$$\dot{\varepsilon}_{zz} = \partial \varepsilon_{zz}/\partial t \tag{26}$$

where $\lambda_{zz} = \frac{\partial z}{\partial Z}$ is the axial stretch.

The fundamental equations, formulated in Lagrangian coordinates, which govern the loading process are given below.

- Mass conservation:

$$\rho_0 = \rho \mathrm{J} \tag{27}$$

  where J is the Jacobian determinant (determinant of the deformation gradient tensor $\mathbf{F}$).

- Momentum balance in the axial direction:

$$\rho_0 \Lambda_0 \frac{\partial^2 w}{\partial t^2} = \frac{\partial}{\partial Z}\left(\frac{\Lambda}{J}\tau_{zz}\right) \tag{28}$$

  where Λ is the current cross-section area of the bar and τ_{zz} is the Kirchhoff stress along the axial direction. For simplicity, from this point on τ_{zz} will be denoted by τ.

- Conservation of energy: in uniaxial stress conditions, Eq. (12) leads to:

$$\rho C_p \frac{\partial T}{\partial t} = k \frac{\partial^2 T}{\partial Z^2} + \beta \tau \mathrm{d}^{\mathrm{p}}_{zz} \tag{29}$$

Consistently with the finite element model of section 5.1, the thermoelastic effects are neglected. Note that, for the sake of simplicity, the spatial derivative which appears in the conductivity term is taken as a Lagrangian derivative.

- Stress rate: according to the stress rate definition used by ABAQUS/Explicit, we adopt the Green-Naghdi objective derivative:

$$\boldsymbol{\tau}^{\nabla} = \dot{\boldsymbol{\tau}} + \boldsymbol{\tau} \cdot \boldsymbol{\Omega} - \boldsymbol{\Omega} \cdot \boldsymbol{\tau} \tag{30}$$

where $\boldsymbol{\Omega} = \dot{\mathbf{R}} \cdot \mathbf{R}^T$ is the spin tensor. Due to the one-dimensional nature of the model, the rotation tensor $\mathbf{R}$ turns into the second order identity tensor $\mathbf{I}$. Then, the objective derivative is computed as a simple time derivative:

$$\boldsymbol{\tau}^{\nabla} = \dot{\boldsymbol{\tau}} \tag{31}$$

Considering the domain $[0, L]$, the equations (27)-(29) and (31) are to be solved under the following initial and boundary conditions formulated in Lagrangian coordinates, which are a one-dimensional form of those defined in section 5.1:

$$\bar{\tau}(Z, 0) = 0; \quad \bar{\varepsilon}(Z, 0) = 0; \quad T(Z, 0) = T_0 \tag{32}$$

$$w\,(0, t) = 0\ ; \quad \dot{w}\,(L, t) = v^{inp} = \dot{\varepsilon}_0 L\ ; \quad \frac{\partial T\,(0, t)}{\partial Z} = \frac{\partial T\,(L, t)}{\partial Z} = 0 \tag{33}$$

6.2. Finite difference model

Relying on the seminal work of Regazzoni et al. (1986), we develop a simple finite difference model to describe the mechanical response of steel bars subjected to dynamic tension. Our explicit numerical approach lies within the spirit of the scheme recently developed by Kudryashov et al. (2015) to investigate the onset and development of shear bands in metallic solids subjected to dynamic loading. In order to construct our numerical solution, we introduce the rectangular grid depicted in Fig. 13 such that $\Pi = \{Z_j = j\Delta Z,\ t^n = n\Delta t\}$, where $j = 0, \ldots, M$ and $n = 0, \ldots, N$. The integration space and time steps are $\Delta Z = L/M$ and Δt respectively.

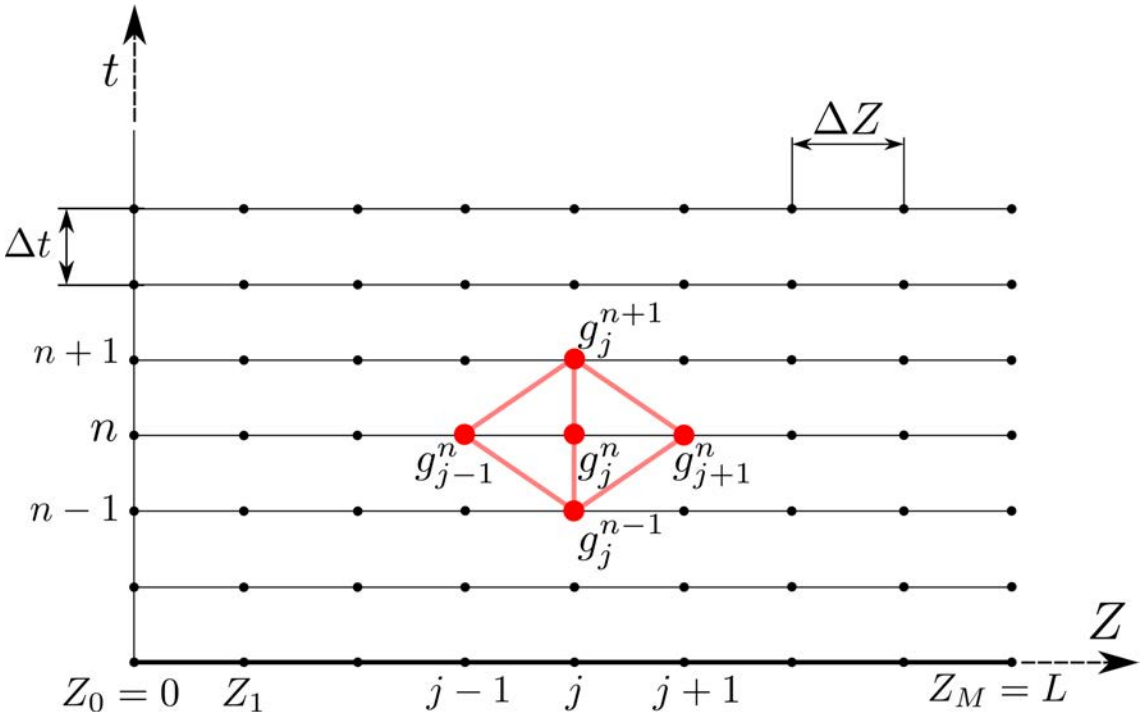

Figure 13: Finite difference model. Grid on time-space domain.

We introduce the following notations of functions in the grid nodes $g\left(Z_j, t^n\right) = g_j^n$. For the first derivative of the functions g with respect to the Lagrangian coordinate Z we have used a central difference discretization which leads to the following second order accuracy approximation:

$$\frac{\partial g}{\partial Z} = \frac{g_{j+1}^n - g_{j-1}^n}{2\Delta Z} \tag{34}$$

Then, the second derivative with respect to the coordinate Z is given by:

$$\frac{\partial^2 g}{\partial Z^2} = \frac{g_{j+1}^n - 2g_j^n + g_{j-1}^n}{\Delta Z^2} \tag{35}$$

For the first order derivative of the functions g with respect to the time t we have used a classical forward difference discretization which leads to the following first order accuracy approximation:

$$\frac{\partial g}{\partial t} = \frac{g_j^{n+1} - g_j^n}{\Delta t} \tag{36}$$

Thus, the second derivative with respect to time t is given by:

$$\frac{\partial^2 g}{\partial t^2} = \frac{g_j^{n+1} - 2g_j^n + g_j^{n-1}}{\Delta t^2} \tag{37}$$

Displacements update

First we solve the kinematics of the problem and update the axial displacement w as a function of the Lagrangian coordinate Z. For that task, we rearrange Eq. (28) to obtain Eq. (38):

$$\begin{aligned}\partial^2 w/\partial t^2 = \mathrm{c}_0^2 \cdot [1 + \partial w/\partial Z]^{-2\gamma} \cdot \Bigg[\frac{\rho}{\rho_0}\Bigg[\Bigg[\frac{\partial^2 w/\partial Z^2}{1 + \partial w/\partial Z}\Bigg][1 - 2\gamma \cdot [\ln(1 + \partial w/\partial Z) - \varepsilon_{zz}^p]] - \\ - \ \partial \varepsilon_{zz}^p/\partial Z\Bigg] + [\ln(1 + \partial w/\partial Z) - \varepsilon_{zz}^p]\frac{1}{\rho_0}\frac{\partial \rho}{\partial Z}\Bigg]\end{aligned} \tag{38}$$

where the following relations have been used:

$$\Lambda = \Lambda_0 \left(1 + \frac{\partial w}{\partial Z}\right)^{-2\gamma} \tag{39}$$

$$\tau = \mathrm{E}\,[\ln(1 + \partial w/\partial Z) - \varepsilon_{zz}^p] \tag{40}$$

where $\mathrm{c}_0 = \sqrt{\dfrac{E}{\rho_0}}$ is the one-dimensional elastic wave speed as a function of the the initial density, E is the Young's modulus, γ is a material parameter and ε_{zz}^p is the plastic strain along the axial direction. Note that Eq. (40) comes from the combination of Eqs. (1), (2) and (3) expressed in one-dimensional form.

Following the discretization scheme defined by Eqs. (34)–(37), Eq. (38) leads to Eq. (41) which allows to update the axial displacement:

$$w_j^{n+1} = [\mathrm{c}_0\Delta t]^2 \left[\frac{2\Delta Z + w_{j+1}^n - w_{j-1}^n}{2\Delta Z}\right]^{-2\gamma} \left[\frac{\rho_j^n}{\rho_0}\left[\left[\frac{2\left(w_{j+1}^n - 2w_j^n + w_{j-1}^n\right)}{\Delta Z\left(2\Delta Z + w_{j+1}^n - w_{j-1}^n\right)}\right]\left[1- \right.\right.\right.$$
$$\left.\left.\left. -2\gamma\left[\ln\left(\frac{2\Delta Z + w_{j+1}^n - w_{j-1}^n}{2\Delta Z}\right) - (\varepsilon_{zz}^p)_j^n\right]\right] - \left(\frac{(\varepsilon_{zz}^p)_{j+1}^n - (\varepsilon_{zz}^p)_{j-1}^n}{2\Delta Z}\right)\right] +$$
$$+\frac{1}{\rho_0}\left(\frac{\rho_{j+1}^n - \rho_{j-1}^n}{2\Delta Z}\right)\left[\ln\left(\frac{2\Delta Z + w_{j+1}^n - w_{j-1}^n}{2\Delta Z}\right) - (\varepsilon_{zz}^p)_j^n\right]\Bigg] + 2w_j^n - w_j^{n-1} \tag{41}$$

Application of Eq. (41) requires to determine the value of γ:

- $\gamma = \nu$ (Poisson's ratio): In the previous time step the material showed purely elastic behaviour.
- $\gamma = 1/2$ (Incompressibility condition): In the previous time step the material deformed elasto-plastically.

Whether $\gamma = \nu$ or $\gamma = 1/2$ is selected for the first time step depends on the impact velocity. If $\rho_0 c_0 v^{inp} < A$, the impact initially induces only elastic strains in the bar (note that A defines the initial yield stress of the material in Eq. (6)) and we take $\gamma = \nu$. If $\rho_0 c_0 v^{inp} \geq A$ the applied velocity induces instantaneous plastic strains in the rod and we take $\gamma = 1/2$.

The stability of the integration procedure is determined by Eq. (41). According to Kudryashov et al. (2015), the numerical scheme is sustainable under the Courant-Friedrisch-Lewy condition:

$$\Delta t \leq \min\left(\frac{\Delta Z}{c_0}\right) \tag{42}$$

The stability and convergence of the finite differences scheme will be shown in section 6.3 and Appendix C.

Stress and temperature update

The stress is updated using a one-dimensional form of the integration scheme developed in section 5.1. Thus, Eq. (15) now reads:

$$\tau^{n+1} = \tau_{\mathrm{trial}}^{n+1} - 2\mathrm{G}\Delta\bar{\varepsilon}^p \tag{43}$$

where the trial stress is given by the following expression:

$$\tau_{\text{trial}}^{n+1} = \tau^n + \eta\left[\Delta\varepsilon_{zz} + 2\Delta\varepsilon_{rr}\right] + 2G\Delta\varepsilon_{zz} \tag{44}$$

where $\Delta\varepsilon_{zz}$ and $\Delta\varepsilon_{rr}$ are the axial and radial strain increments respectively.

The update of the equivalent stress is derived from Eq. (43) and takes the form:

$$\bar{\tau}^{n+1} = \bar{\tau}_{\text{trial}}^{n+1} - 3\text{G}\Delta\bar{\varepsilon}^p \tag{45}$$

The conservation of energy, Eq. (29), is approximated by the following expression which allows to update the temperature of the material as a function of the Lagrangian coordinate:

$$T_j^{n+1} = \frac{k\Delta t}{\rho C_p}\left[\frac{\left(T_{j+1}^n - 2T_j^n + T_{j-1}^n\right)}{\left(\Delta Z\right)^2}\right] + \frac{\beta}{\rho C_p}\bar{\tau}^{n+1}\Delta\bar{\varepsilon}^p + T_j^n \tag{46}$$

In order to obtain the updated stress and the temperature we calculate the equivalent plastic strain increment $\Delta\bar{\varepsilon}^p$ following the procedure previously described in Eqs. (19)–(23).

In the following section we present the results obtained from the finite difference computations. We show comparisons with the experiments and the finite element results reported in sections 4.2 and 5.2, respectively.

6.3. Finite difference results

Fig. 14 shows the normalized axial force $\bar{F}$ as a function of the loading time t for various finite difference computations conducted with four different mesh densities: 150, 200, 250 and 300 nodes. The time step is $\Delta t = 10^9\ s$, the impact velocity $v^{inp} = 16\ m/s$ and the specimen cross-section diameter $\Phi = 3\ mm$. A comparison with a finite element calculation performed under the same loading conditions is presented. Those results indicate that:

1. The predictions of the finite differences scheme are largely insensitive to the mesh density during the process of homogeneous deformation (constant force). On the contrary, the difference is noticeable if we focus on the necking growth rate (rate of decay of the force). In this regard, we note that increasing the number of nodes from 150 to 300 leads to a gradual convergence of the results such that the disagreement between $M = 250$ and $M = 300$ turns to be very small. Thus, we take 300 nodes as the reference mesh density for our finite difference calculations. Note that this combination of mesh density and time step fulfils the stability condition given by Eq. (42). Further evidences on the mesh convergence of the finite difference results are provided in Appendix C.
2. The predictions of the finite difference scheme (from now on we focus the attention on the reference configuration $M = 300$) are largely similar to the finite element calculation during the process of homogeneous deformation. On the contrary, the rate of decay of the force *is much steeper in the case of the finite difference computation.* This issue, the fundamental result that emerges from this analysis, is the following matter of discussion.

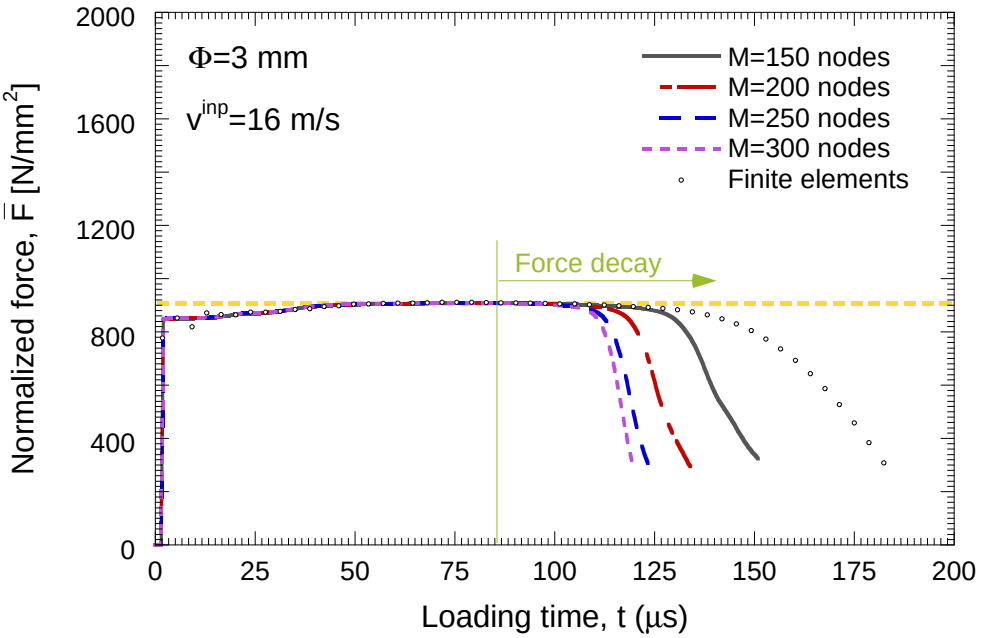

Figure 14: Normalized axial force $\bar{F} = \frac{F}{\Lambda_0}$ as a function of the loading time t. The impact velocity is $v^{inp} = 16\ m/s$ which corresponds to a nominal strain rate $\dot{\varepsilon}_0 = 2000\ s^{-1}$. The specimen cross-section diameter is $\Phi = 3\ mm$. Finite difference results for different mesh densities: $M = 150$, $M = 200$, $M = 250$ and $M = 300$. Comparison with a finite element calculation.

Fig. 15 shows the normalized axial force $\bar{F}$ as a function of the loading time t for finite difference computations conducted with three cross-section diameters: $\Phi = 2\ mm$, $\Phi = 3\ mm$ and

$\Phi = 4\ mm$. The time step is $10^9\ s$, the number of nodes 300 and the impact velocity 16 m/s. Unlike the experiments and the finite element calculations, the $\bar{F} - t$ curves obtained from the finite difference computations do not depend on the specimen cross-section.

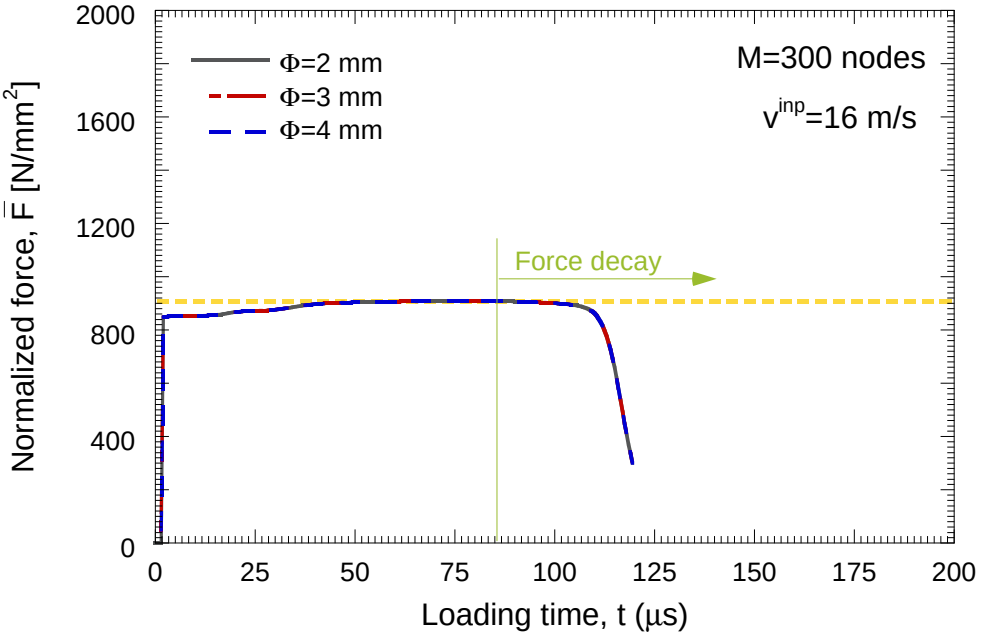

Figure 15: Finite difference results. Normalized axial force $\bar{F} = \frac{F}{A_0}$ as a function of the loading time t for different cross-section diameters: $\Phi = 2\ mm$, $\Phi = 3\ mm$ and $\Phi = 4\ mm$. The impact velocity is $v^{inp} = 16\ m/s$ which corresponds to a nominal strain rate $\dot{\varepsilon}_0 = 2000\ s^{-1}$. The mesh density is $M = 300$ nodes and the time step $\Delta t = 10^9\ s$.

Furthermore, Fig. 16 shows the normalized radial displacement $\bar{u}_a$ versus the loading time t for the same computations presented in (previous) Fig. 15. The $\bar{u}_a - t$ curves practically overlap each other. We observe from the finite difference results that *under uniaxial stress conditions there is no stabilizing effect of the cross-section within the range of strain rates explored.* This is a key outcome of this investigation which illustrates the critical role played by stress multiaxiality in the evolution of necking instabilities in metallic solids subjected to dynamic loading.

In order to elaborate further on the stabilizing role played by the stress mutiaxiality we collect in a single graph (Fig. 17) the normalized growth rate of the neck $\dot{\bar{u}}_a$ (slopes indicated in Figs. 7, 11 and 16) obtained from experiments, finite elements and finite differences.

- Experiments: These experimental results demonstrate that the increase of the cross-section stabilizes the necking instability within the range of strain rates explored in this investigation.

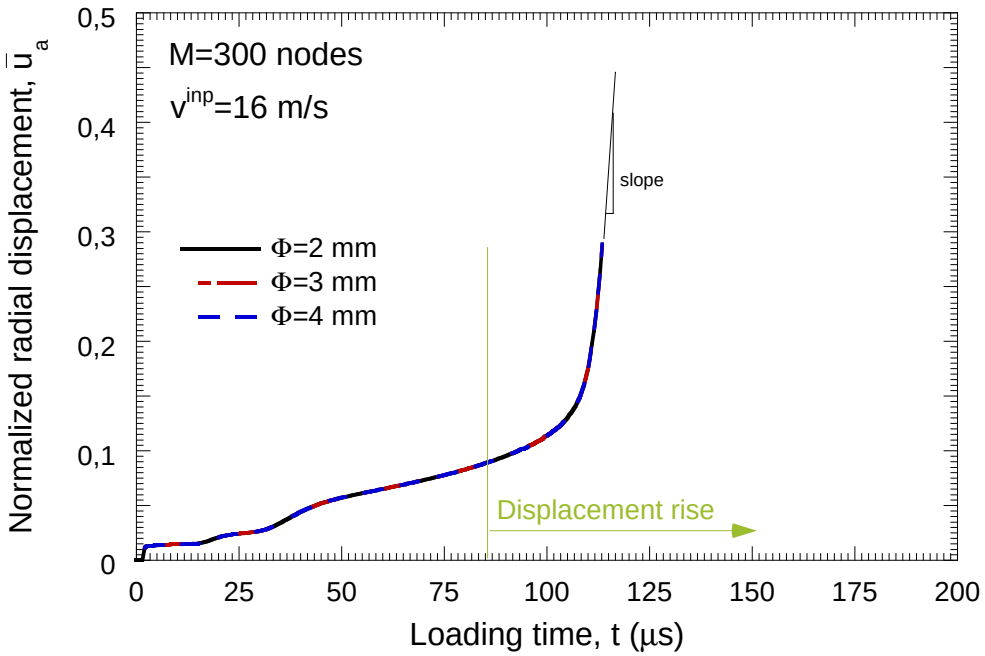

Figure 16: Finite difference results. Normalized radial displacement at the necking location $\bar{u}_a = \frac{2u_a}{\Phi - 2u_a}$ as a function of the loading time t for different cross-section diameters: $\Phi = 2\ mm$, $\Phi = 3\ mm$ and $\Phi = 4\ mm$. The impact velocity is $v^{inp} = 16\ m/s$ which corresponds to a nominal strain rate $\dot{\varepsilon}_0 = 2000\ s^{-1}$. The mesh density is $M = 300$ nodes and the time step $\Delta t = 10^9\ s$.

- Finite elements: According to the experiments, the finite elements predicts a decrease of the necking growth rate with the specimen diameter. The quantitative agreement between the finite elements and the experiments is notable.

- Finite differences: The necking growth rate does not depend on the cross-section diameter. Furthermore, the finite difference scheme predicts much faster necking development than the experiments and finite elements.

We argue that the slowdown of the necking growth rate observed in the experiments and finite elements is caused by the multidimensional character of the flow stress in the necked section. Therefore, the finite difference scheme, due to its one-dimensional nature, cannot capture the stabilizing effect of the cross-section. As discussed by Needleman and Tvergaard (1992), the post-localization stiffness of the specimen is strongly dependent on (geometrical) factors outside the scope of a one-dimensional analysis. On the one hand, flow localization leads to radial and circumferential stresses in the necked section which oppose to the development of the instability (see Appendix B). Furthermore, the evolution of the multiaxial stress state in the necking depends on the specimen diameter. This argument, which stems from the investigations of Bridgman (1944, 1952) and

Le Roy et al. (1981), is supported by the theoretical developments of Fressengeas and Molinari (1985, 1994) and Zhou et al. (2006). This is probably the primary mechanism which slows down the necking growth rate as the cross-section diameter increases. On the other hand, relying on the analytical work of Rubin and Rodríguez-Martínez (2014), we also have to consider the radial inertia as a potential factor contributing to necking stabilization.

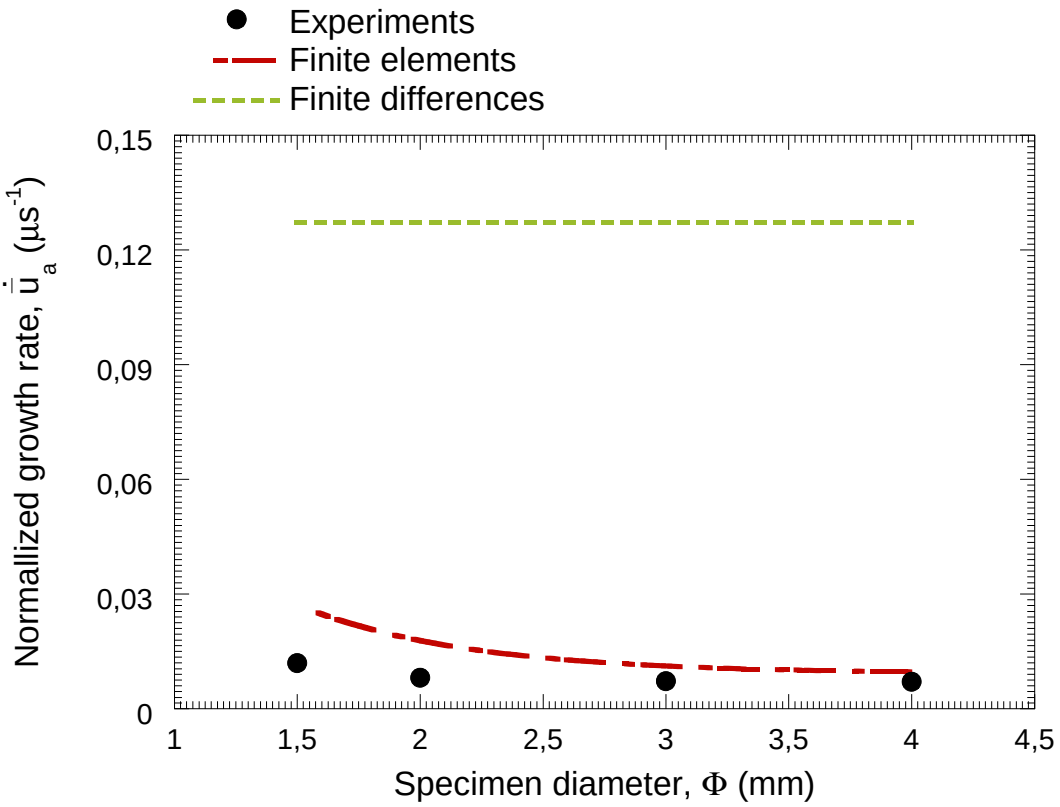

Figure 17: Comparison between experiments, finite elements and finite differences. Normalized growth rate of the neck $\dot{\bar{u}}_a$ versus diameter of the specimen cross-section Φ.

7. Discussion and conclusions

The present work is a joint experimental and numerical effort to quantify and understand the role played by the diameter of cylindrical bars subjected to dynamic loading in the development of necking instabilities. As such, this paper extends to the dynamic regime the celebrated research of Matic et al. (1988). More specifically, we aim at elucidating the influence of the cross-section diameter on the homogenous and post-homogeneous mechanical response of the specimen. The homogeneous deformation case is, as expected, not novel in the sense that as long as the deformation of the bar is homogeneous, the diameter of the bar has a minimal effect on the mechanical

characteristics that can be measured during the test. This goes all the way up to the onset of necking, the latter being barely affected by the bar's diameter, as evidenced both experimentally and numerically (within the range of strain rates explored). The novelty of this work lies, on the one hand, in the experimental characterization of the dynamic development of the neck in the bars, from a quantitative perspective. In a sense, such experiments are in the spirit of those of Bridgman (1944, 1952) who characterized the neck's geometry in statically loaded tensile bars.

The main observation here is that the thinner the bar, the faster the growth of the neck. This is observed repeatedly, and could serve to validate future numerical simulations based on different constitutive models. The second original key point of the work lies in the two-pronged modelling approach used here. Firstly, the axially symmetric finite element simulation, conventional in a way, is shown to closely replicate the experimentally observed trends, namely insensitivity to diameter size in the homogeneous regime, followed by a marked sensitivity of the neck growth speed. However, the second numerical approach of the problem provides a key result. Namely, being a truly one-dimensional analysis, this approach is devoid of stress multiaxiality effects, as opposed to the previous finite element modelling. Therefore, the important outcome of the modelling exercise is that, whereas numerical analyses and experiments are in excellent agreement in the homogeneous deformation regime, in the post localization regime, the finite element results follow closely the experimental ones whereas the one-dimensional analysis predicts an quasi-immediate collapse of the specimen. In other words, the present work clearly demonstrates the important role of the stress multiaxiality on the evolution of a dynamic neck. While such a result was devised theoretically by Fressengeas and Molinari (1985, 1994), Zhou et al. (2006) and Rodríguez-Martínez et al. (2013), the present combined experimental-numerical results are the first, to the authors' knowledge, to confirm earlier works.

It can therefore be concluded that:

1. The growth rate of dynamic necks decreases with the increase of the specimen cross-section.
2. The load drop rate in the post-uniform regime is slowed down with the increase of the sample diameter.
3. The elongation to failure of the bar is strongly dependent on the specimen size.
4. Stress-multiaxiality effects are responsible for the stabilizing character of the specimen cross-

section.

Appendix A. Measurement of the specimen cross-section in dynamic tensile tests

The methodology developed to measure the radial displacement of the necked section consists of the 2 steps illustrated in Fig. A.18 and described below:

1. Determination, resize and upgrade of the area of interest: We assumed that the specimen deforms axisymmetrically in order to focus our attention (only) on half of the sample. The area of interest is enlarged using a bilinear interpolation and upgraded using Photoshop CS6. The resolution of the original and upgraded photographs is 924×768 and 2000×475, respectively.
2. Identification of the current specimen radius using an edge detection technique: We developed a code to assess the contrast of the photograph and identify the contour of the specimen. We scanned each of the vectors making up the photograph and counted the pixels from the axisymmetric axis of the sample to the edge. The minimum number of pixels corresponds to the center of the neck. Since the size of the pixels is known, the number of pixels provides the cross-section diameter of the necked region.

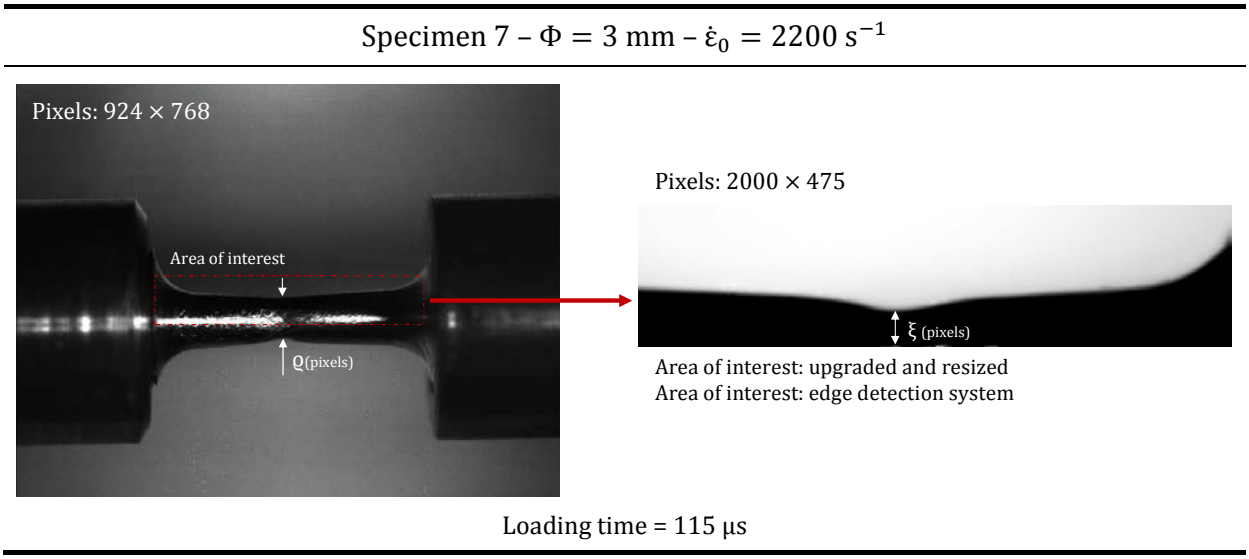

Figure A.18: A procedure to measure the current diameter of the specimen based on the high speed recording of the experiments. Step 1: Determination, resize and upgrade of the area of interest. Step 2: Identification of the current specimen radius using an edge detection technique.

In order to obtain the results illustrated in Fig. 7, this procedure has been applied to all the snapshots that we have obtained from each test.

Appendix B. Stress multiaxiality in the necked section

In this section we provide some additional remarks on the multiaxial stress state of the necked section. We rely on the theoretical framework of Bridgman (1944, 1952) which describes the nonuniform strain and stress distribution in the necked zone of tensile specimens. We acknowledge that Bridgman's analysis was derived for rate and temperature insensitive materials tested under static loading (in this paper we investigate dynamic necking in a thermo-viscoplastic solid). Nevertheless, this simple theoretical framework yields additional insights into the role played by the stress multiaxiality (and the rate of stress multiaxiality) in the necking growth rate.

Fig. B.19 shows a schematic representation of a necked region in an axisymmetric specimen subjected to tensile loading. The current radius of the minimum cross-section is a and the radius of curvature of the neck is Σ. The isostatic lines have been included to illustrate the paths whose tangent is aligned with the direction of the major principal stress, where ω defines the angle between the isostatic lines and the axial direction z. The radius of curvature of the isostatic lines is φ. Note that, in the plane of symmetry $z = 0$, the radial and axial axes coincide with the principal directions.

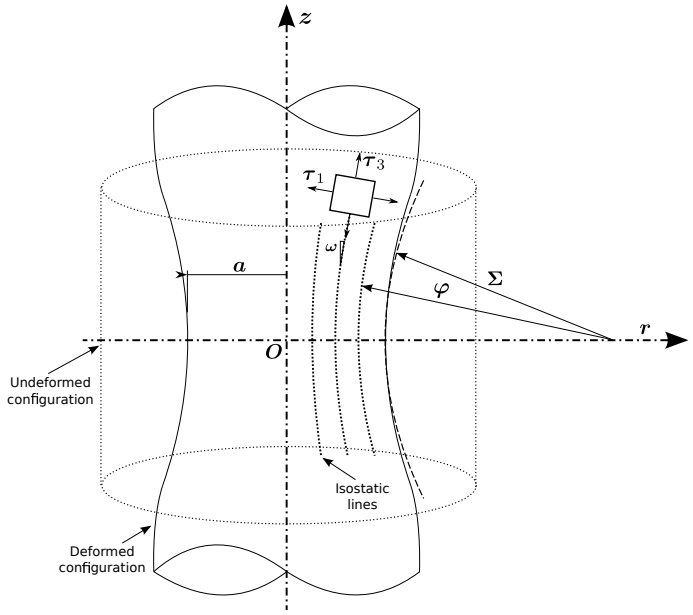

Figure B.19: Schematic representation of a necked region in an axisymmetric specimen subjected to tensile loading.

Strain distribution at the necked section

The deformation rates at the central cross-section of the neck can be written in cylindrical (Eulerian) coordinates $\{r, \theta, z\}$ as:

$$\dot{\varepsilon}_{rr} = \frac{\partial \dot{u}}{\partial r} \; ; \quad \dot{\varepsilon}_{\theta\theta} = \frac{\dot{u}}{r} \; ; \quad \dot{\varepsilon}_{zz} = \frac{\partial \dot{w}}{\partial z} \; ; \quad \dot{\varepsilon}_{r\theta} = \dot{\varepsilon}_{\theta z} = \dot{\varepsilon}_{rz} \tag{B.1}$$

Recall that $\dot{u}$ and $\dot{w}$ are the radial and axial components of the velocity field and the superposed dot denotes differentiation with respect to time. Taking into account the uniformity of the radial strains shown by Bridgman (1944, 1952) and others (Davidenkov and Spiridonova, 1946; Goicolea, 1985; García-Garino et al., 2006), we obtain that:

$$\frac{\partial \dot{u}}{\partial r} = \frac{\dot{u}}{r} \tag{B.2}$$

which leads to:

$$\dot{\varepsilon}_{rr} = \dot{\varepsilon}_{\theta\theta} = \frac{\dot{r}}{r} = \frac{\dot{a}}{a} \tag{B.3}$$

Previous expression is integrated over time taking into account that the radial and circumferential strains are null at $t = 0$:

$$\varepsilon_{rr} = \varepsilon_{\theta\theta} = -\ln\left(\frac{a_0}{a}\right) \tag{B.4}$$

where $a_0 = \frac{\Phi}{2}$ is the initial radius of the cross-section. Further, the incompressibility condition leads to:

$$\varepsilon_{zz} = \bar{\varepsilon} = 2\ln\left(\frac{a_0}{a}\right) \tag{B.5}$$

where $\bar{\varepsilon}$ denotes the Huber-Mises equivalent strain. Moreover, the radial displacement of the free surface of the central cross-section is u_a, such that $a_0 = a + u_a$. Thus, we introduce a dimensionless measure of the radial displacement $\bar{u}_a = \frac{2u_a}{\Phi - 2u_a} = \frac{u_a}{a}$ (see section 4.2) which allows to rewrite the strain components as:

$$\varepsilon_{rr} = \varepsilon_{\theta\theta} = -\ln\left(1 + \bar{u}_a\right) \tag{B.6}$$

$$\varepsilon_{zz} = \bar{\varepsilon} = 2\ln\left(1 + \bar{u}_a\right) \tag{B.7}$$

We differentiate with respect to time Eqs. (B.4) and (B.6) to obtain the following expression which defines the necking growth rate:

$$\dot{\bar{u}}_a = \frac{\dot{a}}{\dot{a}_0}\left(1 + \bar{u}_a\right)^2 \tag{B.8}$$

Stress distribution at the necked section

From the kinematics of the problem it follows that $\tau_{r\theta}$, τ_{rz} and $\tau_{\theta z}$ vanish at the necked section and $\tau_{rr} = \tau_{\theta\theta}$. The analytical expressions for the radial τ_{rr}, circumferential $\tau_{\theta\theta}$ and axial τ_{zz} (simply noted as τ in section 6) stress components were derived by Bridgman (1944, 1952) as a function of the geometrical parameters a and Σ (see Fig. B.19):

$$\tau_{rr} = \tau_{\theta\theta} = \frac{\tau_{avg}}{\left(1 + \frac{2\Sigma}{a}\right)}\left[\frac{\ln\left(\frac{a^2 + 2a\Sigma + r^2}{2a\Sigma}\right)}{\ln\left(1 + \frac{a\Sigma}{2}\right)}\right] \tag{B.9}$$

$$\tau_{zz} = \tau_{\theta\theta} = \frac{\tau_{avg}}{\left(1 + \frac{2\Sigma}{a}\right)}\left[\frac{1 + \ln\left(\frac{a^2 + 2a\Sigma + r^2}{2a\Sigma}\right)}{\ln\left(1 + \frac{a\Sigma}{2}\right)}\right] \tag{B.10}$$

where τ_{avg} is the average stress along the axial direction. Moreover, the Huber-Mises equivalent

stress is:

$$\bar{\tau} = \tau_{zz} - \tau_{rr} = \frac{\tau_{avg}}{\left(1 + \frac{a\Sigma}{2}\right) \ln\left(1 + \frac{a\Sigma}{2}\right)} \tag{B.11}$$

In order to avoid the (complicated) measurement of the neck radius Σ, Bridgman (1944, 1952) proposed the following expression that has been further applied, for instance, by García-Garino et al. (2006):

$$\frac{a}{\Sigma} = \sqrt{\varepsilon_{zz} - 0.1} = \sqrt{2 \ln\left(1 + \bar{u}_a\right) - 0.1} \qquad (\varepsilon_{zz} > 0.1) \tag{B.12}$$

Combining Eqs. (B.9), (B.10), (B.11) and (B.12), and using the dimensionless parameters $\bar{u}_a$ and $\bar{r} = \frac{r}{a}$, we rewrite the stress components as:

$$\tau_{rr} = \tau_{\theta\theta} = \bar{\tau} \ln\left(1 + \frac{1 - \bar{r}^2}{2} \sqrt{2 \ln\left(1 + \bar{u}_a\right) - 0.1}\right) \tag{B.13}$$

$$\tau_{zz} = \bar{\tau} \left[1 + \ln\left(1 + \frac{1 - \bar{r}^2}{2} \sqrt{2 \ln\left(1 + \bar{u}_a\right) - 0.1}\right)\right] \tag{B.14}$$

Note that, in Huber-Mises plasticity, the equivalent stress equals the yield stress $\bar{\tau} = \sigma_Y$, see Eq. (4). Neglecting the viscous and thermal effects (and setting aside the contribution of the elastic strains to the total deformation) the equivalent stress can be written as a function on the equivalent strain $\bar{\tau} \approx g\left(\bar{\varepsilon}\right)$. Taking into account that the equivalent strain $\bar{\varepsilon}$ equals the longitudinal strain ε_{zz} and this, in turn, is sole function of the dimensionless parameter $\bar{u}_a$, we have that the equivalent stress $\bar{\tau}$ is fully defined by the dimensionless parameter $\bar{u}_a$.

This implies that the stress state $\{\tau_{rr}, \tau_{\theta\theta}, \tau_{zz}\}$ at any point of the central cross-section of the neck is fully defined by the parameters $\bar{u}_a$ and $\bar{r}$. Thus, $\bar{u}_a$ and $\dot{\bar{u}}_a$ represent the stress state and the temporal evolution of the stress state in the central cross-section of the neck, respectively.

Appendix C. Additional results on the mesh convergence of the finite differences model

Fig. C.20 shows the current strain rate $\dot{\varepsilon}_{zz}$ as a function of the normalized coordinate $\bar{Z} = \frac{Z}{L}$ for various mesh densities: $M = 150$, $M = 200$, $M = 250$ and $M = 300$. The latter is the reference mesh used in the analysis of section 6.3. The time step is $\Delta t = 10^9\ s$ and the impact velocity $v^{inp} = 16\ m/s$. We have selected the strain rate to check the mesh sensitivity of our calculations because it shows significant fluctuations during the loading processes as a consequence of the propagation and interaction of waves along the bar. Moreover, the strain rate is very sensitive to the spatio-temporal discretization because of its (intrinsic) rate-form definition. As such, it shows very clearly any influence that the discretization may have on the results.

Two different loading times are explored: $t = 13\ \mu s$ in Fig. 20(a) and $t = 52\ \mu s$ Fig. 20(b). The first one $t = 13\ \mu s$ corresponds to an early stage of the loading process in which the strain rate shows significant fluctuations along the sample length. We see that the results converge gradually as we increase the mesh density. The difference between $M = 250$ and $M = 300$ is negligible. Moreover, the second one $t = 52\ \mu s$ corresponds to a later time of the loading process for which the fluctuations of the strain rate are significantly lower. While the disagreement in the results provided by the different meshes is mild, we still observe that mesh *insensitive* results are only achieved if we take $M = 300$.

Acknowledgements

The authors thank Adam Godinger for his technical support.

Stimulating discussions with Alan Needleman and Alain Molinari are acknowledged. We are also indebted to Guadalupe Vadillo, Ramón Zaera and José Fernández-Sáez for many helpful conversations on dynamic instabilities.

The authors of the University Carlos III of Madrid are indebted to the *Ministerio de Economía y Competitividad de España* (Project DPI2014-57989-P) for the financial support which permitted to conduct part of this work.

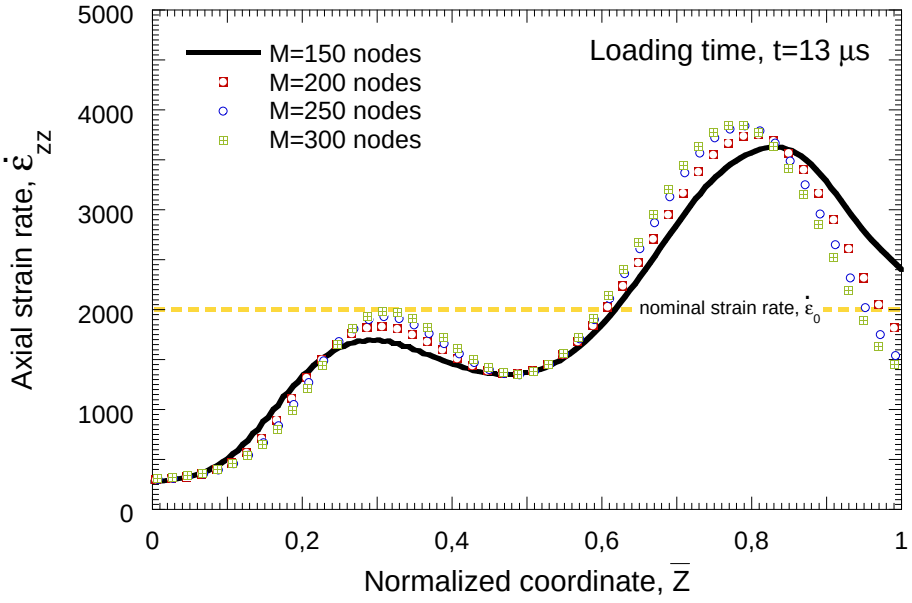

(a)

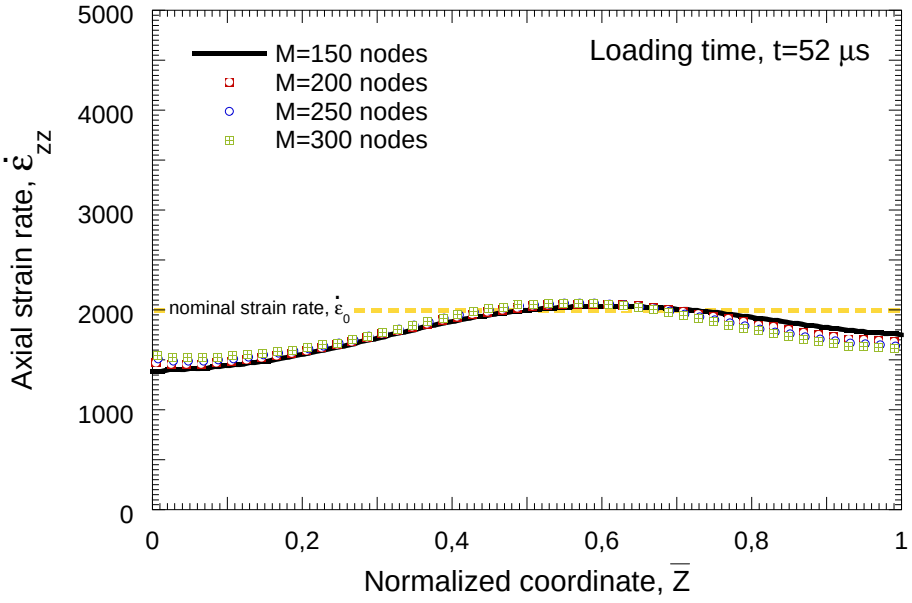

(b)

Figure C.20: Finite difference results. Current strain rate $\dot{\varepsilon}_{zz}$ as a function of the normalized coordinate $\bar{Z} = \frac{Z}{L}$. The impact velocity is $v^{inp} = 16\ m/s$ which corresponds to a nominal strain rate $\dot{\varepsilon}_0 = 2000\ s^{-1}$. Results are shown for different mesh densities: $M = 150$, $M = 200$, $M = 250$ and $M = 300$. Two different loading times are considered: (a) $t = 13\ \mu s$ and (b) $t = 52\ \mu s$.

References

AK steel corporation, 2007. AK steel corporation. Product Data Sheet. 304l stainless steel. 9227 Centre Pointe Drive. West Chester, OH 45069.

Besnard, G., Hild, F., Lagrange, J. M., Martinuzzi, P., Roux, S., 2012. Analysis of necking in high speed experiments by stereocorrelation. International Journal of Impact Engineering 49, 179–191.

Bridgman, P. W., 1944. The stress distribution at the neck of a tensile specimen. Transactions of the American Society of Metals 32, 553–574.

Bridgman, P. W., 1952. Studies in large plastic flow and fracture, with special emphasis on the effects of hydrostatic pressure, vol.1. McGraw-Hill Book Company, Inc., New York.

Clark, D. S., 1942. The Influence of Impact Velocity on the Tensile Characteristics of Some Aircraft Metals and Alloys. Tech. rep., Nationa1 Advisory Committee for Aeronautics.

Clark, D. S., Datwyler, G., 1938. Stress–strain relations under tension impact loading. Proceedings–American Society of Testing Materials 38, 98–111.

Clark, D. S., Duwez, P. E., 1948. Discussion of the forces acting in tension impact test of materials. Journal of Applied Mechanics 15, 243–247.

Considère, A. G., 1885. Mémoire sur l'emploi du fer et de l'acier dans les constructions. Annales des Ponts et Chaussées 9, 574–775.

Davidenkov, N., Spiridonova, N., 1946. Analysis of the state of stress in the neck of a tension test specimen. Proceedings of American Society of Testing Materials 46, 1147–1158.

Davies, E. H., Hunter, D., 1963. The Dynamic Compression Testing of Solids By the Method of the Split Hopkinson Pressure Bar. Journal of the Mechanics and Physics of Solids 11, 155–179.

Doghri, I., 2000. Mechanics of deformable solids: linear and nonlinear, analytical and computational aspects. Springer, Berlin.

Duwez, D. S., Clark, P. E., 1947. An experimental study of the propagation of plastic deformation under conditions of longitudinal impact. Proceedings–American Society of Testing Materials 47, 502–532.

Fressengeas, C., Molinari, A., 1985. Inertia and thermal effects on the localization of plastic flow. Acta Metallurgica 33, 387–396.

Fressengeas, C., Molinari, A., 1994. Fragmentation of rapidly stretching sheets. European Journal of Mechanics A/Solids 13, 251–268.

García-Garino, C., Gabaldón, F., Goicolea, J. M., 2006. Finite element simulation of the simple tension test in metals. Finite Elements in Analysis and Design 42, 1187–1197.

Gilat, A., Schmidt, T. E., Walker, M. F., 2009. Full Field Strain Measurement in Compression and Tensile Split Hopkinson Bar Experiments. Experimental Mechanics 49, 291–302.

Goicolea, J. M., 1985. Numerical modelling in large strain plasticity with application to tube collapse analysis. Ph.D. thesis, University of London.

Guduru, P. R., Freund, L. B., 2002. The dynamics of multiple neck formation and fragmentation in high rate extension of ductile materials. International Journal of Solids and Structures 39, 5615–5632.

Harding, J., Wood, E. O., Campbell, J. D., 1960. Tensile Testing of Materials at Impact Rates of Strain. Journal of Mechanical Engineering Science 2, 488–96.

Hill, R., Hutchinson, J. W., 1975. Bifurcation phenomena in the plane tension test. Journal of the Mechanics and Physics of Solids 23, 239–264.

Hutchinson, J., Neale, K., Needleman, A., 1978. Sheet necking I - validity of plane stress assumptions on the long wavelength approximation. Mechanics of Sheet Metal Forming. Plenum Press, New York, pp. 111–126.

Knoche, P., Needleman, A., 1993. The effect of size on the ductility of dynamically loaded tensile bars. European Journal of Mechanics A/Solids 12, 585–601.

Kolsky, H., 1949. An investigation of the mechanical properties of materials at very high rRates of loading. Proceedings of the Physical Society. Section B 62, 676–700.

Kudryashov, N. A., Ryabov, P. N., Zakharchenko, A. S., 2015. Self-organization of adiabatic shear bands in OFHC copper and HY-100 steel. Journal of the Mechanics and Physics of Solids 76, 180–192.

Le Roy, G., Embury, J. D., Edwards, G., Ashby, M. F., 1981. A model of ductile fracture based on the nucleation and growth of voids. Acta Metallurgica 29, 1509–1522.

Lifshitz, J. M., Leber, H., 1994. Data processing in the split Hopkinson pressure bar tests. International Journal of Impact Engineering 15, 723–733.

Malinowski, J. Z., Klepaczko, J. R., 1986. A unified analytic and numerical approach to specimen behavior in the SHPB. International Journal of Mechanical Sciences 28, 381–391.

Mann, H. C., 1936. High-velocity tension-impact tests. Proceedings–American Society of Testing Materials 36, 85–109.

Mann, H. C., 1937. Fundamental study of the design of impact test specimens. Proceedings–American Society of Testing Materials 37, 102–130.

Matic, P., Kirby III, G. C., Jolles, M. I., 1988. The relation of tensile specimen size and geometry effects to unique constitutive parameters for ductile materials. Proceedings of the Royal Society of London. Series A, Mathematical and Physical Sciences 417, 309–333.

Mercier, S., Molinari, A., 2003. Predictions of bifurcations and instabilities during dynamic extensions. International Journal of Solids and Structures 40, 1995–2016.

Mercier, S., Molinari, A., 2004. Analysis of multiple necking in rings under rapid radial expansion. International Journal of Impact Engineering 30, 403–419.

Mirone, G., 2013. The dynamic effect of necking in Hopkinson bar tension tests. Mechanics of Materials 58, 84–96.

Molinari, A., 1997. Collective behaviour and spacing of adiabatic shear bands. Journal of the Mechanics and Physics of Solids 45, 1551–1575.

Needleman, A., 1988. Material rate dependence and mesh sensitivity in localization problems. Computer Methods in Applied Mechanics and Engineering 67, 69–85.

Needleman, A., 1991. The effect of material inertia on neck development. Topics in Plasticity. AM Press, Ann Arbor, MI, pp. 151–160.

Needleman, A., Tvergaard, V., 1992. Analyses of plastic flow localization in metals. Applied Mechanics Reviews 45, S3–S18.

Nemes, J. A., Eftis, J., 1993. Constitutive modelling on the dynamic fracture of smooth tensile bars. International Journal of Plasticity 9, 243–270.

Noor, A. K., Needleman, A., Peters, J. M., 1998. Sensitivity analysis for failure and damage in dynamically loaded tensile bars. Computer Methods in Applied Mechanics and Engineering 151, 461–478.

Osovski, S., Rittel, D., Rodríguez-Martínez, J. A., Zaera, R., 2013. Dynamic tensile necking: Influence of specimen geometry and boundary conditions. Mechanics of Materials 62, 1–13.

Regazzoni, G., Johnson, J. N., Follansbee, P. S., 1986. Theoretical Study of the Dynamic Tensile Test. Journal of Applied Mechanics 53, 519–528.

Rittel, D., Rotbaum, Y., Rodríguez-Martínez, J. A., Sory, D., Zaera, R., 2014. Dynamic necking of notched tensile bars: An experimental study. Experimental Mechanics 54, 1099–1109.

Rodríguez-Martínez, J. A., Pesci, R., Rusinek, A., 2011. Experimental study on the martensitic transformation in AISI 304 steel sheets subjected to tension under wide ranges of strain rate at room temperature. Materials Science and Engineering: A 528, 5974–5982.

Rodríguez-Martínez, J. A., Vadillo, G., Fernández-Sáez, J., Molinari, A., 2013. Identification of the critical wavelength responsible for the fragmentation of ductile rings expanding at very high strain rates. Journal of the Mechanics and Physics of Solids 61, 1357–1376.

Rotbaum, Y., Osovski, S., Rittel, D., 2015. Why does necking ignore notches in dynamic tension? Journal of the Mechanics and Physics of Solids 78, 173–185.

Rotbaum, Y., Rittel, D., 2014. Is there an optimal gauge length for dynamic tensile specimens? Experimental Mechancics 54, 1205–1214.

Rubin, M. B., Rodríguez-Martínez, J. A., 2014. The effect of radial inertia on flow localization in ductile rods subjected to dynamic extension. International Journal of Impact Engineering 69, 157–164.

Sato, K., Qiang, Q., Hiramoto, J., Urabe, T., Yoshitake, A., 2015. A method to investigate strain rate effects on necking and fracture behaviors of advanced high-strength steels using digital imaging strain analysis. International Journal of Impact Engineering 75, 11–26.

Shenoy, V. B., Freund, L. B., 1999. Necking bifurcations during high strain rate extension. Journal of the Mechanics and Physics of Solids 47, 2209–2233.

Simó, J. C., Hughes, T. J. R., 1998. Computational Inelasticity. Springer, New York.

Simulia, 2010. ABAQUS/Explicit User's Manual, version 6.10 Edition. Dassault Systèmes, Providence, USA.

Sørensen, N. J., Freund, L. B., 1998. Dynamic bifurcation during high-rate planar extension of a thin rectangular block. European Journal of Mechanics A/Solids 17, 709–724.

Tarigopula, V., Hopperstad, O. S., Langseth, M., Clausen, A. H., Hild, F., 2008. A study of localisation in dual-phase high-strength steels under dynamic loading using digital image correlation and FE analysis. International Journal of Solids and Structures 45, 601–619.

Tvergaard, V. R., Needleman, A., 1990. Damage mechanics in engineering materials. Vol. 109 of . ASME, Ch. Ductile failure modes in dynamically loaded notched bars, pp. 117–128.

Xue, Z., Vaziri, A., Hutchinson, J. W., 2008. Material aspects of dynamic neck retardation. Journal of the Mechanics and Physics of Solids 56, 93–113.

Zaera, R., Fernández-Sáez, J., 2006. An implicit consistent algorithm for the integration of thermoviscoplastic constitutive equations in adiabatic conditions and finite deformations. International Journal of Solids and Structures 43, 1594–1612.

Zaera, R., Rodríguez-Martínez, J. A., Casado, A., Fernández-Sáez, J., Rusinek, A., Pesci, R., 2012. A constitutive model for analyzing martensite formation in austenitic steels deforming at high strain rates. International Journal of Plasticity 29, 77–101.

Zaera, R., Rodríguez-Martínez, J. A., Rittel, D., 2013. On the Taylor-Quinney coefficient in dynamically phase transforming materials. Application to 304 stainless steel. International Journal of Plasticity 40, 185–201.

Zhou, F., Molinari, J. F., Ramesh, K. T., 2006. An elasto-visco-plastic analysis of ductile expanding ring. International Journal of Impact Engineering 33, 880–891.

Zukas, J. A., Scheffer, D. R., 2000. Practical aspects of numerical simulations of dynamic events: effects of meshing. International Journal of Impact Engineering 24, 925–945.